Microstructure and properties of hard and optically transparent HfO_2 films prepared by high-rate reactive high-power impulse magnetron sputtering

by

NAI-WEN PI

Presented to the Faculty of the Graduate School of

The University of Texas at Arlington in Partial Fulfillment

of the Requirements

for the Degree of

MASTER OF SCIENCE IN MATERIALS SCIENCE AND ENGINEERING

THE UNIVERSITY OF TEXAS AT ARLINGTON

May 2016

Copyright © by Nai-Wen Pi 2016

All Rights Reserved

Acknowledgements

I would like to thank all of those who have helped and supported me in any respect during the completion of this research. First, I would like to express my deepest appreciation to my advisor Dr. Jiechao Jiang for his guiding, instructions, patience and support to both my research and adaption to life in Arlington, Texas. And I would like to express my sincere gratitude to our department chair Dr. Efstathios I. Meletis for his support and suggestion to my master research. I also want to acknowledge my committee member Dr. Fuqiang Liu for his time and suggestions.

I would also like to thank Dr. J. Vlček and his group from University of West Bohemia providing thin film samples fabricated using high-power impulse magnetron sputtering. I would like to acknowledge my group senior member Ms. Minghui Zhang for her countless help, encouragement, support and friendship.

I am also grateful to MSE staff, Ms. Jennifer Standlee, Ms. Beth Robinson and Mr. David Yan, who have been always more than helpful in many aspects for completing my master program.

April 14, 2016

Abstract

Microstructure and properties of hard and optically transparent HfO_2 films prepared by high-rate reactive high-power impulse magnetron sputtering

Nai-Wen Pi, MS

The University of Texas at Arlington, 2016

Supervising Professor: Jiechao Jiang

Hafnium Dioxide (HfO_2) has an extraordinary high bulk modulus, high hardness, high chemical stability, high melting point and high thermal stability. This material can be used as protective coatings for application involving high temperature environments. HfO_2 films were fabricated on Si using high-rate reactive high-power impulse magnetron sputtering (HiPIMS) using different deposition-averaged target power density $<S_d>$ and voltage pulse durations t_1. Five HfO_2 films were prepared with (1) t_1 = 25 μs, $<S_d>$ =7.6 Wcm^{-2} (T25S7), (2) t_1 = 100 μs, $<S_d>$ =7.2 Wcm^{-2} (T100S7), (3) t_1 = 200 μs, $<S_d>$ =7.3 Wcm^{-2} (T200S7), (4) t_1 = 200 μs, $<S_d>$ =18 Wcm^{-2} (T200S18) and (5) t_1 = 200 μs, $<S_d>$ =54 Wcm^{-2} (T200S54).

Atomic force microscopy (AFM) images of the T200S54, T200S18 and T200S7 films exhibit a coarser granular structure with a similar grain size varying from 25 nm to 120 nm in

diameter and an average grain size of ~70 nm. AFM images of the T25S7 and T100S7 films show smaller granular structures compared to the other three films.

Transmission electron microscopy (TEM) studies show that all films are composed of an interlayer next to the Si interface followed by a nano-columnar structure layer. The interlayer structure of the films consists of a population of lower density nanoscale regions. A reduction in t_1 and $<S_d>$ in films T200S54, T200S18, T200S7 and T100S7 caused an increase in the interlayer thickness and a decrease in the width of the nano-columnar structures from ~46 nm to ~21 nm. This microstructural change was accompanied by a concomitant change of the grain boundary structure from tight and interlocking in films T200S54 and T200S18, to rough and thicker (~1 nm) boundaries in films T200S7 and T100S7. Film T25S7 exhibited an entirely different microstructure composed of a multilayered interlayer (~3 nm) and nano-columnar (~15 nm) structure. Films prepared with large t_1 (200 μs) have a monoclinic HfO_2 structure and that with small t_1 **(**25 μs) an orthorhombic HfO_2 structure. Film prepared with an intermediate t_1 value (100 μs) exhibited a mixture of both monoclinic and orthorhombic phases. A high hardness of 17.6-17.0 GPa was shown for films with a monoclinic HfO_2 structure. The films exhibited a refractive index of 2.02-2.11 and an extinction coefficient between ≤$2x10^{-3}$ and $0.1x10^{-3}$ (both at a wavelength of 550 nm). High optical quality was achieved for films T200S54 and T200S18 owing to the presence of a dense microstructure with sharp and interlocking grain boundaries.

Table of Contents

Acknowledgements iii

Abstract…. iv

List of Illustrations viii

List of Tables xi

Chapter 1 Introduction 1

1.1 Motivation 2

1.2 Research Objectives 4

1.3 Dissertation Overview 4

Chapter 2 THIN FILMS SYNTHESIS AND CHARACTERIZATION 6

2.1 Synthesis of Hafnium dioxide Thin Films 6

2.2 Thin Film Characterization Techniques 7

2.2.1 X-ray diffraction 7

2.2.2 Atomic force microscopy 8

2.2.3 Nano-indentation 11

2.2.4 Transmission electron microscopy 15

2.3 TEM Sample Preparation 16

2.3.1Cross-section TEM sample preparation 16

2.3.2 Plan-view TEM Sample Preparation 17

2.3.3 Focus ion beam (FIB) Cross-section TEM sample preparation 18

Chapter 3 MICROSTRUCTURE OF HfO_2 FILMS DEPOSITED ON (100) Si SUBSTRATE . 20

3.1 X-ray diffraction result 20

3.2 Atomic force microscopy result 25

3.3 Nano-indentation result 26

3.4 Transmission electron microscopy result 28

3.4.1 T25S7 sample 28

3.4.2 T200S54 and T200S18 sample 32

3.4.3 T200S7 and T100S7 sample 37

3.5 Influence of deposition parameters on microstructure and properties 42

Chapter 4 CONCLUSION 46

References 48

List of Illustrations

Figure 2.1 Schematic illustration showing basic steps for cross-section TEM sample preparation. 16

Figure 2.2 Schematic illustration showing the plan-view TEM sample preparation procedure. 18

Figure 3.1 XRD θ-2θ scan of the HfO2 thin film deposited on Si substrate. 20

Figure 3.2 Non-contact AFM 3D images of HfO2 films (a) T200S54, (b) T200S18, (c) T200S7, (d) T100S7 and (e) T25S7. 26

Figure 3.3 (a) Force vs. Displacement curves. (b), (c), (d) the indentation image from T200S54, T100S7 and T25S7 27

Figure 3.4 Illustration for cross-section and plan view TEM imaging 29

Figure 3.5 (a) and (b) Bright-field cross-section TEM image and SAED (inset) of the T25S7 film and the film/Si substrate interface, respectively. (c) and (d) plan-view TEM image taken from the T25S7 film and the film/Si interface, respectively. 30

Figure 3.6 (a) and (b) cross-section HRTEM image of the T25S7 taken from the film and the film/Si interface, respectively. (c) and (d) Plan-view HRTEM image taken from an area in Fig. 3.5 (c) and (d), respectively. 31

Figure 3.7(a) and (b) Plan-view TEM image, (c) and (d) SAED pattern of the T200S54 and T200S18 film, respectively. 33

Figure 3.8 (a) and (d) Cross-section TEM image of the HfO_2 film taken from T200S54 and T200S18, respectively. (b) and (d) SAED pattern taken from the HfO_2 film in T200S54 and T200S18, respectively. (c) and (f) Cross-section TEM image of the film/Si interface in T200S54 and T200S18, respectively. 34

Figure 3.9 (a) and (b) Cross-section HRTEM image of the HfO_2 film and film/Si interface in T200S54, respectively. (c) Magnified cross-section TEM and (d) HRTEM image of the interface between the HfO_2 columnar structure and the interlayer in T200S18. 36

Figure 3.10 (a) and (b) Plan-view TEM image for T200S7 and (b) T100S7, respectively. (c) SAED pattern of the T100S7 film in a plan-view TEM foil. (d) Comparison of SAED pattern for the T200S7 and T100S7 film. 38

Figure 3.11 (a, c) and (b, d) Cross-section TEM image and SAED pattern of the HfO_2 film from T200S7 and T100S7, respectively. (e) and (f) TEM image of the film/Si interface for T200S7 and T100S7, respectively. 40

Figure 3.12 (a) Cross-section HRTEM image of the HfO_2 film in T200S7. (b) and (c) HRTEM image of the interface between HfO_2 columnar structure and HfO_2 interlayer in T200S7. (d) HRTEM image of the interface between the HfO_2 interlayer and Si in T100S7. 42

Figure 3.13 (a) Variation of column width in the HfO_2 thin films as a function of voltage pulse duration (t_1) and target power density ($<S_d>$). (b) Variation of column width with $(t_1<S_d>)^{1/2}$. 43

Figure 3.14 (a) Variation of interlayer thickness in the HfO_2 thin films with voltage pulse duration (t_1) and target power density ($<S_d>$). (b) Variation of k_{550} with $t_1/<S_d>$ and interlayer thickness. 44

List of Tables

Table 3.1.1 Comparison of the XRD data between m-HfO_2, o-HfO_2, t-HfO_2 and c-HfO_2 21

Table 3.1.2 T25S7 XRD θ-2θ peaks....... 22

Table 3.1.3 T200S54 XRD θ-2θ peaks 23

Table 3.1.4 T200S18 XRD θ-2θ peaks 23

Table 3.1.5 T200S7 XRD θ-2θ peaks 24

Table 3.1.6 T100S7 XRD θ-2θ peaks 25

Table 3.3 mean hardness and effective Young's modulus 27

Table 3.4 List of the d-spacing of the m-HfO_2, o-HfO_2, and the measured values from the SAED patterns of the T200S54, T200S18, T200S7 and T100S7. 39

Chapter 1

Introduction

Hafnium Dioxide (HfO_2) have attracted increasing interesting due to relatively high refractive index and wide band gap [1,2]. It is technologically important because of its extraordinary high bulk modulus, high melting point, and high chemical stability, as well as its high neutron absorption cross section [3]. As a dielectric material, it can be used in protective coatings because of its thermal stability and hardness, which makes them very promising candidates for application involving high temperature environments [4]. In addition, HfO_2, as a high-k dielectric material, has also been investigated as tunneling oxide or blocking oxide to achieve fast program/erase speed for nonvolatile memory application and developed as gate dielectric to improve gate control ability for low-temperature poly-Si thin-film transistors [5]. In nowadays, HfO_2 is used to replace silica (SiO_2) as the insulator in order to increase chip performance and cut down on electron leakage. While the optical behavior is well-known, very few attention has been paid to the microstructure and mechanical properties [6,7].

Reactive dc magnetron sputtering [8-14] and various pulsed magnetron sputtering [15-17] techniques have been used to deposit HfO_2 films. High-power impulse magnetron sputtering (HiPIMS) with a pulsed reactive gas flow control was recently developed for high-rate reactive depositions of densified, highly optically transparent, stoichiometric HfO_2 films onto floating substrates [18]. The depositions were performed using a strongly unbalanced

magnetron with a directly water-cooled planar Hf target in argon-oxygen gas mixtures. With this method, the HfO_2 films can be fabricated with very high deposition rates (up to 200 nm/min) even at an averaged target power density of approximately 30 Wcm^{-2}. The latter is relatively close to a target power density applicable in industrial HiPIMS systems. The HfO_2 films prepared using this technique were hard and exhibited a hardness up to 18 GPa, a refractive index of 2.07-2.12 and an extinction coefficient between ≤ $0.1x10^{-3}$ and $0.6x10^{-3}$ at the wavelength of 550 nm.

In this work, we have employed high-resolution TEM and electron diffraction to study the microstructure of five selected representative hard and optically transparent HfO_2 films prepared by high-rate HiPIMS [18]. The motivation for this work was to develop an understanding of the processing-microstructure-property relationship of these films as a function of the deposition parameters of averaged target power density ($\langle S_d \rangle$) and voltage pulse durations (t_1).

1.1 Motivation

Hafnium dioxide (HfO_2) has become an important coating material due to its attractive properties. They include high melting point (~ 2800 °C) and excellent thermal stability, high refractive index and low absorption over a broad region (from the near-UV, ~250 nm to the mid-IR, >12 μm), high dielectric constant and high neutron absorption cross section [19]. HfO_2 can

find a wide range of applications (semiconductors, optical devices, nuclear industries and coating technologies). For example, HfO_2-based materials have been explored as thermal barrier coatings for turbine blades operating in harsh and high-temperature environments [20, 21]. HfO_2 films can be used as visible, near-IR and mid-IR antireflection coatings [22-24], UV mirrors with a high damage threshold [25], heat mirrors for energy-efficient windows [26] and chirped mirrors and band pass filters [8]. HfO_2 is also considered to be one of the most promising candidates to replace SiO_2 on Si in gated electronic devices [27].

High power impulse magnetron sputtering (HIPIMS) is a technique that lately has drawn attention from both industry and academia [28]. High power impulse magnetron sputtering (HIPIMS) is an emerging physical vapor deposition (PVD) technology that has previously shown enhancement of thin film quality [29-31]. It is characterized by a high pulse power density at the sputtering target, which is typically two orders of magnitude greater than the average power density [32]. The main advantages of HIPIMS coatings include a denser coating morphology [33]. However, the use of HIPIMS to grow higher-order material systems, for instance ternary compounds, is yet to be investigated. [34] As a suitable candidate for such ambitions, we choose HfO_2.

1.2 Research Objectives

In this work, the microstructures, interfaces and self-organized growth evolution of hafnium dioxide (HfO_2) thin films deposited on (100) Si substrate using magnetron sputtering was primarily studied.

The overall objective of the present research is to develop an understanding of the growth deposition parameters on the microstructure of monoclinic and orthorhombic hafnium dioxide (HfO_2) based thin films. The current research work has focused on the following specific objectives:

(i) To investigate the microstructure of HfO_2 thin film deposited on (100) Si substrate using DC magnetron sputtering and provide fundamental knowledge for the growth of HfO_2 thin films.

(ii) To study the microstructure and interfaces between different sputtering conditions (different deposition time and power density)

1.3 Dissertation Overview

This dissertation consists of four chapters. An outline and summary of each chapter is summarized as follows.

Chapter 1, Introduction: This chapter introduces the motivation and objectives of this research work. It also provides a brief idea about HfO_2 thin films and the necessity of studying, developing and designing the barium HfO_2 thin films.

Chapter 2, Thin Film Synthesis and Characterization: This chapter describes the detail deposition system set up and deposition parameters for HfO_2 thin films. The characterization techniques in terms of high-resolution transmission electron microscopy (HRTEM), X-ray diffraction (XRD), atomic force microscopy (AFM), Nanoindentation tests are explained.

Chapter 3, Microstructure of HfO_2 films deposited on (100) Si substrate: This chapter is going to present the HfO_2 films microstructure analysis result from high-resolution transmission electron microscopy (HRTEM), X-ray diffraction (XRD), atomic force microscopy (AFM), Nanoindentation. And also present the summary with these five HfO_2 thin films.

Chapter 4, Conclusions: In this chapter, the major results and discussions, and the directions for future work are included.

Chapter 2

THIN FILMS SYNTHESIS AND CHARACTERIZATION

Hafnium dioxide (HfO_2) thin films were fabricated on (100) Si substrates using DC magnetron sputtering. The HfO_2 films were deposited onto Si substrates at a floating potential using a strongly unbalanced magnetron source with a directly water-cooled planar hafnium target (99.9 % Hf purity, diameter of 100 mm and thickness of 6 mm) in a standard stainless-steel vacuum chamber. The details of the deposition conditions for each film are introduced in this chapter. The microstructures of the thin films were characterized in details using HRTEM, XRD, AFM, and nanoindentation as described in the following section.

2.1 Synthesis of Hafnium dioxide Thin Films

The HfO_2 films were deposited onto Si substrates at a floating potential using a strongly unbalanced magnetron source with a directly water-cooled planar hafnium target (99.9 % Hf purity, diameter of 100 mm and thickness of 6 mm) in a standard stainless-steel vacuum chamber. The target-to-substrate distance was 100 mm. An external heater was used during depositions and the substrate temperature ranged from 140 to 165 °C. The target surface temperature was kept under 350 °C by using water cooling [21]. The base pressure before deposition was 10^{-3} Pa and a reactive gas (oxygen) was admitted into the vacuum chamber from a source via mass flow controllers and two corundum conduits for deposition. The total

pressure of the argon–oxygen gas mixtures was kept close to 2 Pa with a measured accuracy of ~ 1 %. The magnetron was driven by a high-power pulsed dc power supply (HMP 2/1, Hüttinger Elektronik). The repetition frequency (fr) was 500 Hz. The range for t1 was from 25 to 200 μs and for $<S_d>$ from 7.2 to 54 Wcm-2. A detailed description of the film deposition parameters is given in Ref. [20]. Five films were prepared in this work for detailed microstructure characterization with (1) t_1 = 25 μs, $<S_d>$ =7.6 Wcm^{-2} (named as T25S7); (2) t_1 = 100 μs, $<S_d>$ =7.2 Wcm^{-2} (T100S7); (3) t_1 = 200 μs, $<S_d>$ =7.3 Wcm^{-2} (T200S7); (4) t_1 = 200 μs, $<S_d>$ =18 Wcm^{-2} (T200S18) and (5) t_1 = 200 μs, $<S_d>$ =54 Wcm^{-2} (T200S54).

2.2 Thin Film Characterization Techniques

2.2.1 X-ray diffraction

The structure and phase purity of the films were studied using Bruker D8 Advance X-ray diffractometer. A Cu Kα radiation source with the wavelength of 1.54056 Å, was used at an acceleration voltage and filament current of 40 kV and 40 mA, respectively. The Basic settings were scan from 10 degree to 60 degree. The scanning speed was 1 mins per degree with overnight repeat scanning (above 6 hours). The main scanning type in this project was using θ-2θ scan. The XRD θ-2θ was determined by Bragg's law:

$$2d \sin \theta = n\lambda$$

Here d is the spacing between diffracting planes, θ is the incident angle, n is any integer, and λ is the wavelength of the beam. If scatters are arranged symmetrically with a separation d, these spherical waves will be in sync (add constructively) only in directions where their path-length difference 2d sin θ equals an integer multiple of the wavelength λ. These specific directions appear as spots on the diffraction pattern called reflections. Thus, X-ray diffraction results from an electromagnetic wave (the X-ray) impinging on a regular array of scatters (the repeating arrangement of atoms within the crystal).

2.2.2 Atomic force microscopy

For the morphology analysis we chose AFM to do it. The AFM has two major abilities: force measurement and imaging. The surface roughness and morphology of the as-deposited films were characterized using a Park systems' XE 70 AFM. Non-contact mode was used in this work. In force measurement, AFMs can be used to measure the forces between the probe and the sample as a function of their mutual separation. This can be applied to perform force spectroscopy.

For imaging, the reaction of the probe to the forces that the sample imposes on it, can be used to form an image of the three-dimensional shape (topography) of a sample surface at a high resolution. This is achieved by raster scanning the position of the sample with respect to the tip and recording the height of the probe that corresponds to a constant probe-sample

interaction (see section topographic imaging in AFM for more details). The surface topography is commonly displayed as a pseudocolor plot.

All steps for nano-indentation will be presented in below.

1. Remove the XE head: Detach the Head cable -> Unlock the Dove Tail locks -> Slide the head out.
2. Prepare sample for imaging: Mount the sample on a sample disk using super glue or adhesive tap -> Place the sample disk on the sample holder.
3. Prepare tip for imaging: Place a chip carrier with a mounted cantilever on to the XE Head
4. Install the XE Head: Slide the head in -> Lock the Dove Tail locks -> Connect the Head cable -> Turn on the beam
5. Load XEP and vision software: Turn on the Control Electronics -> Run uEye software -> Run XEP software
6. Align the beam to make the beam reflect off the cantilever head and into center of PSPD; Using camera Panning Screws and Focus knob to find the cantilever on uEye -> Using the Beam Align Screws to move the beam onto the head of the cantilever -> Using the PSPD Align Screws to center the reflected beam on the PSPD (Adjusting the PSPD Align Screw until the A+B approaching to the maximum value (over 2V) and then centering the beam to the cross point, A-B<0.5V and C-D<0.5V)

7. Select Head Mode and set point in XEP: Turn off the Head in the XEP software by clicking the Laser Off button -> Click the Part Select button to open XEP Part selection menu -> Select the Head mode, such as C-AFM and NC-AFM, and cantilever; making sure that the Head mode selected matches the mounted cantilever type -> Select “HIGH” for XY Voltage Mode and Z Voltage mode, if the sample surface is not very flat and the scan area is not very small (<1 μm) -> Turn on the Head after confirming the settings: NC-AFM mode and C-AFM mode.
8. Create session/filename for the images to be saved: Open the Tools submenu in XEP window -> Select Session Manager, create a session name and location for the images to be saves -> Select Preference, create a filename in the Filename Format area
9. Approach tip to sample: Click on the bottom part of the Z Motor Control until the distance between the tip and sample surface is within several mm (monitored by naked eye) -> Move the Focus down until you see the sample surface. Move the XY stage until you find the area you wish to image -> Move the Z stage down slowly until the sample cantilever begins to come into focus (the cantilever is quit close to sample) -> Click the Approach button, and the cantilever will move down until the set point met.
10. Adjust scan parameters: Click the “input” button and select the inputs that you wish to calculate and save while imaging. For C-AFM: Usually select Topography and Error Signal. For NC-AFM: Usually select Topography, Error Signal, NC Amplitude, and NC Phase. ->

Select a nonzero scan size, trace line windows will open -> Adjusting scan parameters to make the forward and the backward trace lines match in the topography trace window -> Click “Start Scan” to acquire an image.

2.2.3 Nano-indentation

Nano-indentation tests can provide a direct and continuous measurement of dynamic indentation hardness and modulus varying with penetration depth of the thin films. In nano-indentation, small loads and tip sizes are used, so the indentation area may only be a few square micrometres or even nanometres.

Nano-indentation measurements were performed in a Hysitron Ubi 1 Nanomechanical Test Instrument to investigate the mechanical properties of the selected thin films. A three-sided pyramid Berkovich diamond tip was used in the measurements. The elastic modulus and hardness values were obtained by providing corresponding forces with the same displacement of 75 nm on each film.

Sixteen indents in a 4×4 array with spot-spot distance of 3 μm within a total area of 9×9 um^2 were selected to determine the average hardness and Young’s modulus of the films.

All steps for nano-indentation will be presented in below.

1. Sample prepaeation: nano-indenter can handle sample size of ~1 cm^2. If the sample is larger than this, cut it to fit on the disk. Mount the sample on the puck using a small amount of super glue.

2. Open the Acoustic Enclosure and place the sample on the sample stage: place the sample/disk near the edge on the stage. Slide the disk towards the middle position and the strong magnet in the center of the stage will hold the disk in place.
3. Use the micrometers on the stage to roughly align the sample under the tip (Be very careful Never accidentally touch the tip, even slightest contact will damage the tip)
4. Turn on the computer and monitor
5. Turn on (1) Z-axis motor controller; (2) Piezo controller; and (3) Transducer controller in that order. The reverse order is used during shutdown.
6. Adjust the "DISPLAY GAIN" to "1
7. Check the original LOAD value on the Front Panel. It should be about -350
8. Press "Auto Zero" button on (3)
9. Zero the front panel meter by manually adjusting the coarse button to less than 0.01
10. Open the program on computer "TRIBOSCAN"
11. At this point a dialog box will appear in the center of the screen, you can either click Cancel or allow the clock to expire to start the program, or you can click Analysis Only to use the analysis program without starting the machine
12. After Zero and open the program, it will show "please reset/adjust the front-panel meter to zero" on the screen.

13. Push “Auto Zero” Button more time and use Course & Fine knob to adjust the front- panel meter to zero.
14. Click “OK” on the screen
15. Press CALIBRATION tab
16. Under “System Calibration” menu, in the area of System Setup, change the Front Panel Setting (on computer): Low Pass Filter (Hz): 300; Displacement Gain: 100; Microscope Feedback Gain: 100
17. Also change the relevant Front Panel Setting on Transducer Controller (Low Pass Filter (Hz): 300; Displacement Gain: 100; Microscope Feedback Gain: 100) to match the values on computer
18. In the ”Transducer Calibrations” area, press Calibrate button under Indentation Axis
19. Click Cal Air Indent
20. Click Start button
21. Re-zero LOAD value on the Front Panel Setting on Transducer controller. Then click OK button
22. Double click Front Panel Setting on Transducer Controller (Low Pass Filter (Hz): 300; Displacement Gain: 100; Microscope Feedback Gain: 100) and click OK button.
23. “Do you want to keep this in your Air Calibration Indent data”? Click Yes Button. The Calibration for Scratch Axis follow the same step 18-23

24. Re-zero LOAD value on the Front Panel Setting on Transducer Controller; change the Displacement Gain to 1000; Microscope Feedback to 1000 on the Front Panel Setting of Transducer Controller. (Pop-up says output but bring both 1000. The low pass filter should remain “300” do not touch!)
25. Change the relevant Front Panel Setting in System Setup on computer (Low Pass Filter (Hz): 300; Displacement Gain: 1000; Microscope Feedback Gain: 1000) to match the values on Transducer Controller.
26. Go to Sample Navigation
27. Select Mode: Indentation or Scratch
28. Turn on the camera switch
29. Adjust the sample position: (a) click Z Safety DISABLE icon (become RED); (b) point the mouse to “+Z” position and hold the left button of the mouse. The tip will be lowering down. Bring the tip close to the sample
30. Click Z Safety DISABLE icon again (become gray)
31. Press Create Boundary and click OK button
32. Press “quick approach”, then OK and let it run
33. Go Imaging; Max scan size is 60μm X 60μm; this will allow multiple indentation space. When you increase the scan size, the velocity increase (you don’t want). Keep the velocity

<30μm/sec. Once you change the value, click the mouse outside, wait: Default scan rate: 1 Hz

34. Click sample approach
35. Press “GO” and wait! (Start scan for imaging)
36. If there is an overall slope, we can correct it by going to “IMAGE”, background subtraction -> choose linear regression -> press “CLOSE”
37. To save images, go to “IMAGE”. CAPTURE: File name (find out the folder) Give name, say OK -> press “CAMERA” next to “STOP”
38. Press “Load Function” , Press QUASI -> File—open Load function -> choose trapezoid.ldf -> Load; Once the graph comes: press on any line to change -> press “Loading” -> peak force;: 5000μN

2.2.4 Transmission electron microscopy

High resolution TEM (Hitachi H-9500 operated at 300 KV) was used to record selected area electron diffraction (SAED) patterns and some high magnification bright field TEM images. The point resolution of the TEM is 1.8 Å. Both cross-section and plan-view TEM samples were investigated by HRTEM. The cross-section TEM observation can provide important information of the interface between the substrate and the film which closely relate to the mechanism of the film crystal nucleation, growth, defect and strain, as well as the orientation relationships. The

plan-view TEM observation could supply more information along the top view of the film, which provides critical structural information that is lacking from cross-section TEM.

SAED patterns were also took in the HRTEM. The crystal d-spacing can be measured from EDP or Fast Fourier Transformation (FFT) of the HRTEM image using a Gatan's Digital Micrograph software installed in Hitachi H-9500 HRTEM.

2.3 TEM Sample Preparation

2.3.1Cross-section TEM sample preparation

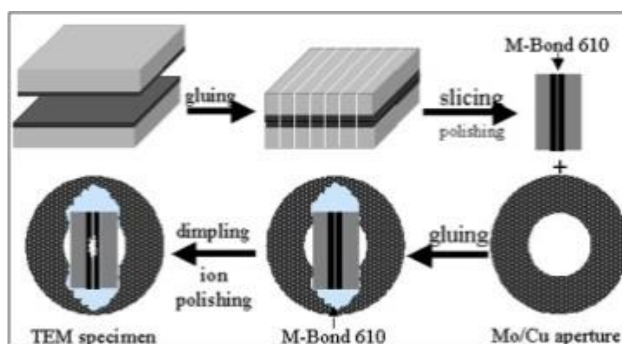

Figure 2.1 Schematic illustration showing basic steps for cross-section TEM sample preparation.

The procedure of plan-view TEM sample preparation is shown in Figure 2.1. The steps involved are:

1. Cut two 1 mm × 3 mm rectangular pieces from sample along a specific direction using low speed diamond saw.

2. Glue these two as-cut slides face to face by joining the film side using M-bond 610 adhesive after cleaning with acetone and Ethanol. And then put it on the heater (120 ℃) for 20 mins.

3. Polishing the sample on the cross section side sequentially conducted on diamond lapping films from 30 μm, 15 μm to 6 μm 3 μm to 1 μm.

4. Mount the polished side of the sample on a 3 mm copper ring and then grind using 1000 grit sand paper to gradually reduce the thickness of the sample into 60 μm thickness.

5. Place the sample on a precision dimple grinder and polish the sample using copper wheel, remove 40 μm thickness away in the middle. And using fiber wheel with Al polishing solution to polish for 20 mins.

6. Using the Ar-ion mill system named Gatan model 691 precise ion polishing system (PIPS) to reduce the sample thickness (4 degree polishing angle) until there is a hole produced close to the film area. The edges of the hole could be thin enough for TEM investigation

2.3.2 Plan-view TEM Sample Preparation

The procedure of plan-view TEM sample preparation is shown in Figure 2.2. The steps involved are:

1. Cut a 2×2 mm sample piece using the diamond saw.

2. Glue the as-cut slide on a 3 mm diameter copper ring with the film side facing down using M-bond 610 adhesive and put it on the heater (120 ℃) for 20 mins.

3. Polish the sample using a 1000 grit sand paper (decrease the thickness to 60 μm).

4. Place the sample on a precision dimple grinder and polish the sample using copper wheel, remove 40 μm thickness away in the middle area. And using fiber wheel with Al polishing solution to polish the sample for 20 mins.

5. Use an Ar-ion milling PIPS to gradually reduce the sample thickness until there is a hole showing up on the sample. The thin areas close to hole edges could be good for later TEM investigation.

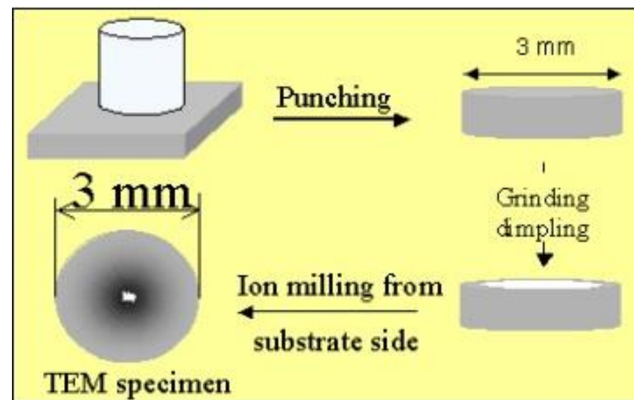

Figure 2.2 Schematic illustration showing the plan-view TEM sample preparation procedure.

2.3.3 Focus ion beam (FIB) Cross-section TEM sample preparation

1. Clean the sample surface with Acetone and Ethanol.

2. Put the sample on the FIB holder and then install the holder into FIB chamber.

3. Find the sample in the E-beam image, and focus on the sample surface -> do height calibration (Z axis) under focus image -> adjust the Z axis working distance to 5 mm

4. Do alignment in I-beam and E beam: find a calibration point (such as defect or crack) and tilt the stage from 0 degree to 5 degree. Moving the stage height to do calibration, make the image back to focus on calibration point. Do this step with several times. When the calibration point remain the same position, we can tilt the angle into working angle, which is 52 degree and so calibration again. Check both I-beam and E beam image to adjust the image into same position.

5. Stop scanning the image and open the AUTO TEM software. Set up the width, thickness and depth for TEM sample after that we can click start.

6. The sample preparation will start automatically: First, it will etch two “X” marks on the sample surface as auto calibration point. Than the I-beam will deposit a thin Pt coating on sample preparation area. After deposited Pt step, the I-beam will start to remove two rectangle regions (etching from 50.5 and 53.5 degree) and there will remain a thin film region between these two rectangle regions. When the thin film was formed, the stage will tilt to 10 degree and etch a “J” shape cut.

7. After the Auto TEM sample preparation, we have to input the nanoprob to help us move the TEM foil to TEM sample holder. We will stick the TEM foil on nanoprob by deposition Pt, and cut the rest “J” shape so the TEM foil can be remove away from sample surface.

8. Find the TEM sample holder position, and operate the nanoprob in order to put TEM foil on TEM sample holder.

Chapter 3

MICROSTRUCTURE OF HfO_2 FILMS DEPOSITED ON (100) Si SUBSTRATE

3.1 X-ray diffraction result

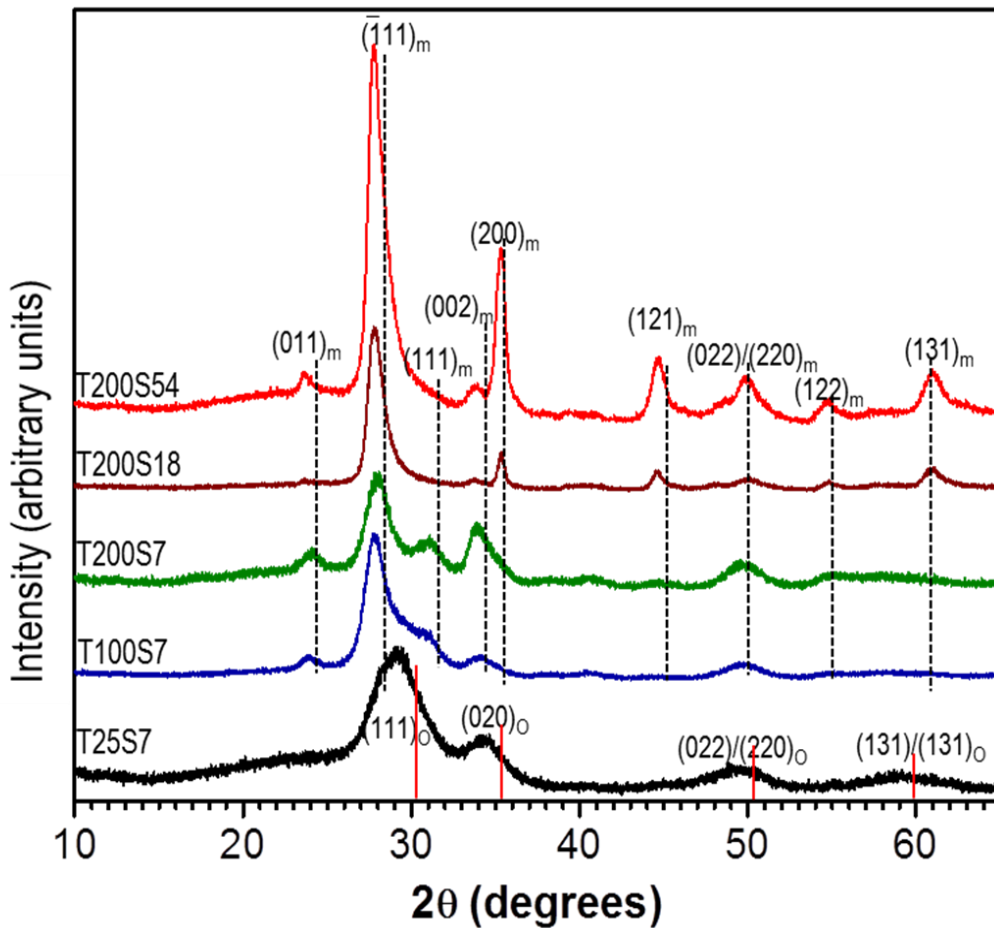

Figure 3.1 XRD θ-2θ scan of the HfO_2 thin film deposited on Si

We examined the crystal structure of the films using θ-2θ XRD (Fig 3.1). It should be noted that HfO_2 has been reported to have four possible crystal structures: monoclinic, orthorhombic, tetragonal (t-HfO_2, PDF#: 08-0342: a= 5.14 Å, c=5.25 Å, P42/nmc) [35] and cubic (fcc, a=5.11 Å) [19]. Table 3.1.1 summarizes the XRD data of monoclinic, orthorhombic,

tetragonal and cubic structure. “x” indicates the indices of the peak were not given in the PDF file.

d (Å)	Monoclinic			Orthorhombic			Tetragonal			Cubic (a=5.11Å)		
	h	k	l	h	k	l	h	k	l	h	k	l
5.051	1	0	0									
5.007				1	0	1						
3.677	0	1	1									
3.612	1	1	0	1	1	1						
3.24				0	0	2						
3.146	-1	1	1									
2.97							x	x	x			
2.95				1	0	1				1	1	1
2.825	1	1	1									
2.79				0	1	2						
2.622							0	0	2			
2.614	0	0	2	0	2	0						
2.603				1	1	1						
2.584	0	2	0									
2.555							2	0	0	2	0	0
3.529				0	0	2						
2.527	2	0	0									
2.504				2	0	0						
2.489	-1	0	2									
2.356							1	0	2			
2.332	0	1	2	0	2	1						
2.317	0	2	1	1	2	0						
2.301	1	2	0									
2.270	2	1	0									
2.258				2	1	0						
2.243	-1	1	2									
2.201	-2	1	1									
2.184	1	0	2									
2.165	-1	2	1									

Table 3.1.1 Comparison of the XRD data between m-HfO_2, o-HfO_2, t-HfO_2 and c-HfO_2

The XRD pattern of the film T25S7 exhibits four diffraction peaks at 2θ angle of 29.11°, 34.21°, 49.37° and 59.03° corresponding to lattice spacing of 3.06 Å, 2.62 Å, 1.84 Å and 1.56 Å, respectively (Table3.1.2). Those peaks can be identified as the (111), (020), (022)/(220) and (131)/(113) of the orthorhombic HfO_2 (o-HfO_2, PDF #: 01-070-2832, a= 5.0073 Å, b=5.2276 Å, c=5.058 Å, Pbcm) [35]. Formation of the orthorhombic HfO_2 phase has been reported in the literature [10]. The diffraction peaks of film T25S7 are broad due to small grain size. A closer examination shows that due to their proximity, these peaks also fit the corresponding {111}, {200} and {220} diffractions of the tetragonal and cubic HfO_2 structure. Thus, the T25S7 film structure cannot be distinguished from the XRD without ambiguity.

T25S7							
2θ (°)	d(Å)	(hkl) of o-HfO_2	Height	I%	Area	I%	P/N
29.11	3.065	111	227	100	24619	100	3.3
34.21	2.619	200	119	52.4	12523	50.9	2.5
49.37	1.844	022	34	15	4064	16.5	0.9
59.03	1.564	113	34	15	3551	14.4	1

Table 3.1.2 T25S7 XRD θ-2θ peaks

The XRD pattern from the T200S54 film exhibits peaks at 2θ° positions of 23.62°, 27.76°, 33.74°, 35.34°, 44.66°, 49.94°, 54.76° and 60.92° corresponding to lattice spacing of 3.76 Å, 3.21 Å, 2.65 Å, 2.54 Å, 2.03 Å, 1.82 Å, 1.67 Å, 1.52 Å, respectively (Table 3.1.3). The XRD pattern from the T200S18 film exhibits peaks at 2θ° positions of 23.62°, 27.69, 33.81, 35.32, 44.64, 50.05, 54.83, and 60.83 corresponding to lattice spacing of 3.76 Å, 3.21 Å, 2.65

Å, 2.54 Å, 2.03 Å, 1.82 Å, 1.67 Å and 1.52 Å, respectively (Table 3.1.4). Those T200S54 and T200S18 peaks can be identified as the (011), ($\bar{1}$11), (002), (200), (121), (022)/(220), (122) and (131) of the monoclinic HfO_2 structure (m-HfO_2, PDF #: 01-075-6426, a= 5.1187 Å, b=5.1693 Å, c=5.297 Å, β=99.18°, P21/c) [35].

T200S54							
2θ (°)	d (Å)	(hkl) of m-HfO_2	Height	I%	Area	I%	P/N
23.62	3.764	110	255	5.5	8973	3.7	4
27.76	3.211	-111	4659	100	243408100	100	31
33.74	2.654	002	167	3.6	6580	2.7	2.9
35.34	2.538	200	2081	44.7	70187	28.8	19.9
44.66	2.027	-202	745	16	31618	13	10.7
49.94	1.825	220	339	7.3	16602	6.8	5.5
54.76	1.675	202	217	4.7	9824	4	4.4
60.92	1.519	-302	467	10	22691	9.3	7.2

Table 3.1.3 T200S54 XRD θ-2θ peaks

T200S18							
2θ (°)	d (Å)	(hkl) of m-HfO_2	Height	I%	Area	I%	P/N
23.62	3.763	011	49	2.5	2853	1.3	1.7
27.69	3.219	-111	1986	100	217562	100	21
33.81	2.649	002	72	3.6	4393	2	2.5
35.32	2.539	200	443	22.3	21629	9.9	9.3
44.64	2.028	112	221	11.1	15916	7.3	6.2
50.05	1.821	220	95	4.8	8888	4.1	3.1
54.83	1.673	202	94	4.7	6630	3	3.5
60.83	1.522	113	212	10.7	18659	8.6	5.5

Table 3.1.4 T200S18 XRD θ-2θ peaks

The XRD patterns of the T200S7 film exhibits peaks at 2θ° positions of 24.08°, 27.9°, 31.03°, 33.9°, 49.7° and 54.76° corresponding to lattice spacing of 3.69 Å, 3.19 Å, 2.88 Å, 2.64 Å, 1.83 Å and 1.67 Å, respectively (Table 3.1.5).

T200S7							
2θ (°)	d (Å)	(h k l) of m-HfO_2	Height	I%	Area	I%	P/N
24.08	3.693	011	120	27.3	10346	22.3	3.2
27.90	3.195	-111	440	100	46320	100	7.4
31.03	2.880	111	128	29.1	11704	25.3	3.1
33.90	2.642	002	266	60.5	24852	53.7	5.7
40.50	2.226	-211	50	11.4	2376	5.1	1.8
58.39	1.579		46	10.5	1496	3.2	1.6

Table 3.1.5 T200S7 XRD θ-2θ peaks

The XRD patterns of the T100S7 exhibits peaks at 2θ° positions of 23.93°, 27.78°, 34.01°, 40.54°, 49.76° and 54.74°corresponding to lattice spacing of 3.72 Å, 3.21 Å, 2.63 Å, 2.22 Å, 1.83 Å and 1.68 Å, respectively (Table 3.1.6). Those T200S7 and T100S7 peaks can be identified as the (011), ($\bar{1}$11), (111), (002), (022) and (122) of the m-HfO2 structure [35]. Thus, the films prepared with large t_1 exhibit a monoclinic structure whereas those films with the short t_1 exhibit a different structure (orthorhombic, tetragonal or cubic).

All diffraction peaks are shifted toward lower angle of 2θ, compared with the standard values probably caused by the high compressive stress in the film.

T100S7							
2θ (°)	d (Å)	(h k l) of m-HfO_2	Height	I %	Area	I %	P/N
23.93	3.716	011	137	11.8	12723	10.3	3.3
27.78	3.209	-111	1158	100	123497	100	12.6
34.01	2.634	002	130	11.2	13083	10.6	3.1
40.54	2.223	-211	44	3.8	4504	3.6	1.5
49.76	1.831	220	98	8.5	9604	7.8	2.7
54.74	1.675	202	30	2.6	2323	1.9	1.1

Table 3.1.6 T100S7 XRD θ-2θ peaks

3.2 Atomic force microscopy result

The surface morphology and roughness of five HfO_2 films were investigated using AFM in the non-contact mode with a scanning size of 1×1 μm^2. Figs.3.2 (a), (b) and (c) show 3D AFM images of films T200S54, T200S18 and T200S7, respectively, exhibiting a coarser granular structure. The structures in the three films have a similar grain size varying from 25 nm to 120 nm in diameter with an average size of ~70 nm. Figs.3.2 (d) and (e) are 3D AFM images of films T100S7 and T25S7, respectively, showing smaller granular structures compared to the former three films. The granular structures in the films T100S7 and T25S7 have a size varying from 20 nm to 80 nm, whereas the average size is ~45 nm for T100S7 and ~30 nm for T25S7. All films were smooth and the average mean roughness (R_a) was ~0.66 nm, 1.07 nm, 0.60 nm, 0.85 nm and 0.82 nm for films T200S54, T200S18, T200S7, T100S7 and T25S7, respectively.

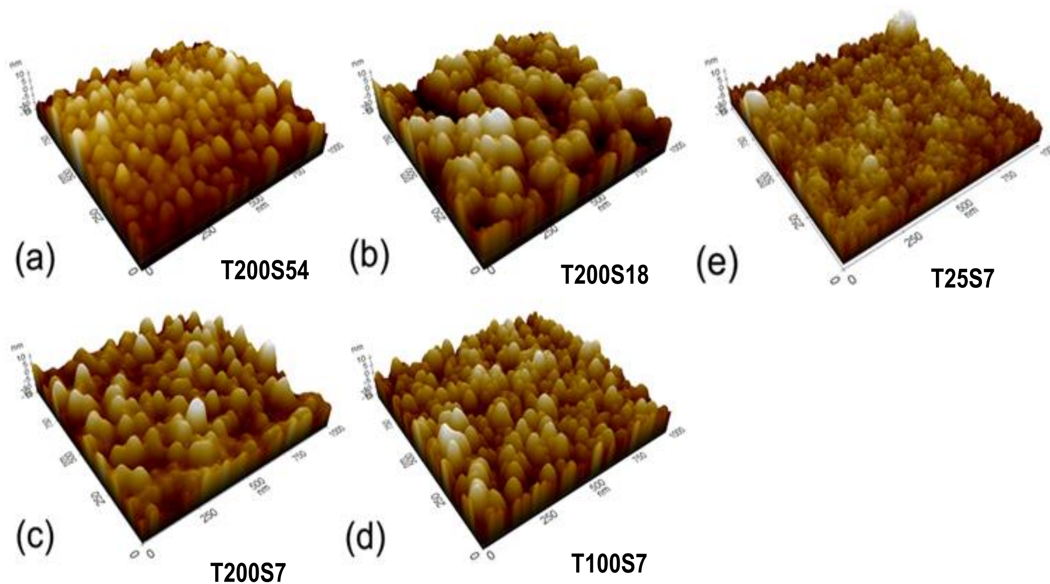

Figure 3.2 Non-contact AFM 3D images of HfO2 films (a) T200S54, (b) T200S18, (c) T200S7, (d) T100S7 and (e) T25S7.

3.3 Nano-indentation result

We have conducted nano-indentation experiments to study the film hardness and Young's modulus. Fig. 3.3(a) shows typical Force vs. Displacement curves for the five films. The mean hardness and effective Young's modulus of the T200S54, T200S18, T200S7, T100S7 and T25S7 HfO_2 film were 17.6/176.8, 17.5/176.5, 15.0/176.0, 13.4/162.0 and 10.1/137.9 GPa, respectively. The values of H and E* of the five films are summarized in Table 3.3. Figs. 3.3(b) - (d) show typical images of the indentations on the T200S54, T100S7 and T25S7 films. A clear difference in the indentation size between the T200S54 and T25S7 film is discerned while films T200S18 and T200S7 exhibited nearly the same size as that of the T200S54 film. These hardness values are consistent with films prepared previously with HiPIMS [18] and higher than those reported in the literature (e.g., 12-15 GPa) [19].

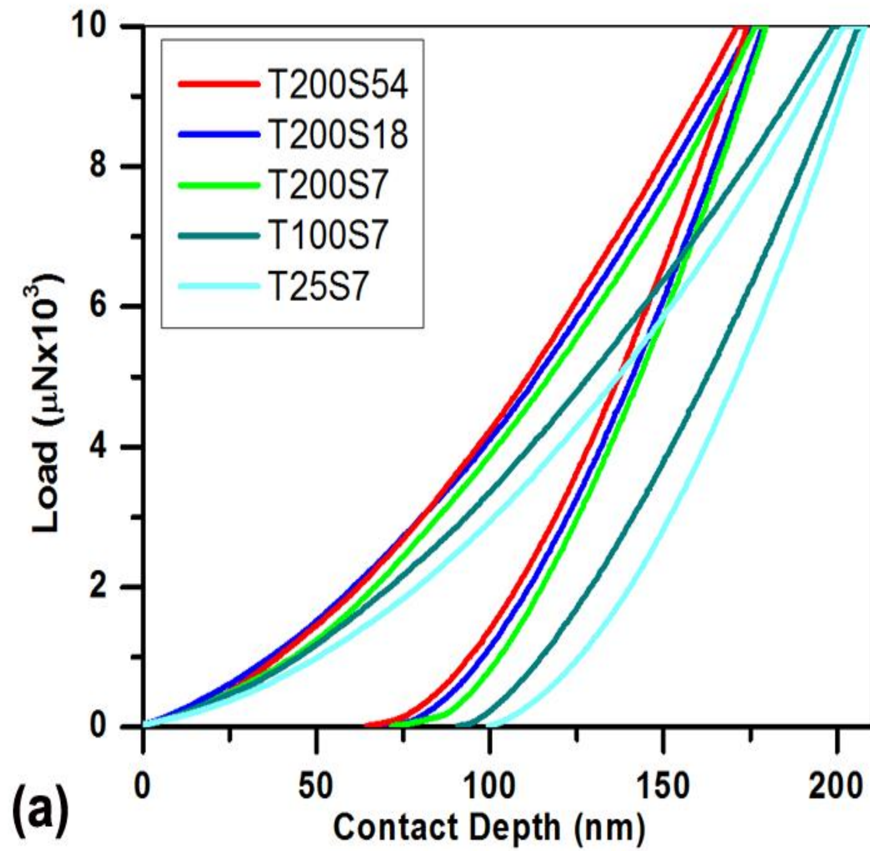

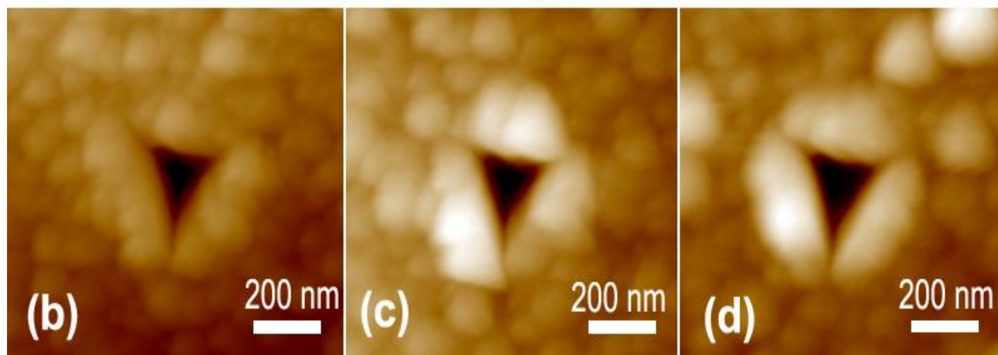

Figure 3.3 (a) Force vs. Displacement curves. (b), (c), (d) the indentation image

from T200S54, T100S7 and T25S7

Film No.	Hardness (GPA)	Modulus (GPa)
T200S54	17.6	176.8
T200S18	17.5	176.5
T200S7	17.0	176.0
T100S7	13.4	162.0
T25S7	10.1	137.9

Table 3.3 mean hardness and effective Young's modulus

3.4 Transmission electron microscopy result

The detail microstructure of the films was studied using cross-section and plan-view TEM (Fig.3.4). The cross-section TEM images of all five films show a very uniform and smooth film surface and a sharp interface with the Si substrate. The T200S54, T200S18, T200S7, T100S7 and T25S7 film thickness obtained from the cross-section TEM measurements was about 1000 nm, 1100 nm, 1000 nm, 960 nm and 1000 nm, respectively. All films were composed of an interlayer with the Si substrate followed by a nano-columnar structure layer with hilly boundary. The interlayer was fully occupied by nano-cavities. The microstructure of the HfO_2 films viewed from a cross-section direction was shown in figure 3.4.

3.4.1 T25S7 sample

The microstructure of T25S7 films was investigated using TEM. Fig 3.5 (a) is a cross-section TEM image from the upper region of sample. In this picture, the columnar structure can be seen clearly. The width for each columnar is around 15 nm. The upper left corner shows the selected-area electron diffraction (SAED) pattern taken from the columnar structure. The five diffraction rings 1, 2, 3, 4 and 5 in SAED pattern correspond to a lattice spacing of 3.61 Å, 2.94 Å, 2.55 Å, 1.81 Å and 1.55 Å, respectively. These rings can be identified as the (110), (111), (020)/(002), (022)/(220) and (131) of the o-HfO_2 (PDF #: 01-070-2832).

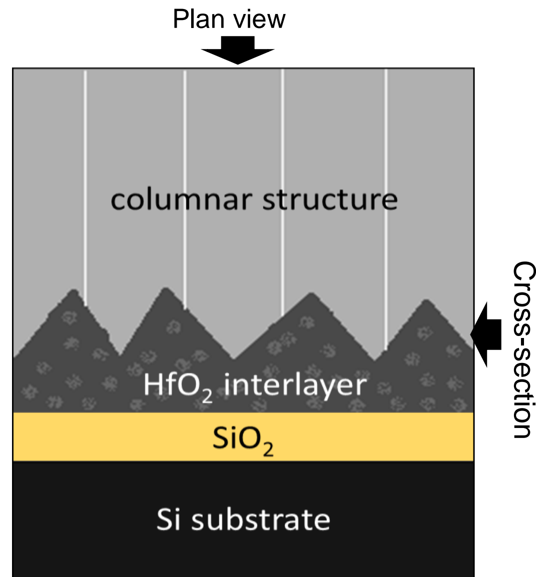

Figure 3.4 Illustration for cross-section and plan view TEM imaging

Fig 3.5 (b) is a cross-section TEM image taken from the area above the Si substrate. A multilayered structure can be seen and the thickness for each layer is around 5 nm. The faint columnar structure present in Fig. 3.5 (a) is no more visible in Fig. 3.5 (b). SAED patterns in Figs. 3.5 (a) & (b) show that the film region near the interface exhibits the same crystal structure as that away from the interface. Both of SAED patterns were identified as o-HfO_2 phase structure. The regions right above the four-layered structure, such as B_1 and B_2, appear brighter than the region above them (such as F). This contrast different is not due to the crystallographic orientation change or thickness different, but made by density different. Fig. 3.5 (c) is the plan view TEM image which was taken from the surface area of the HfO_2 coating. The grain boundary can be clearly seen and the average grain size was measured around 20 nm. Fig 3.5

(d) is plan-view TEM image taken from low portion area above the substrate indicating formation of porous structure in this area.

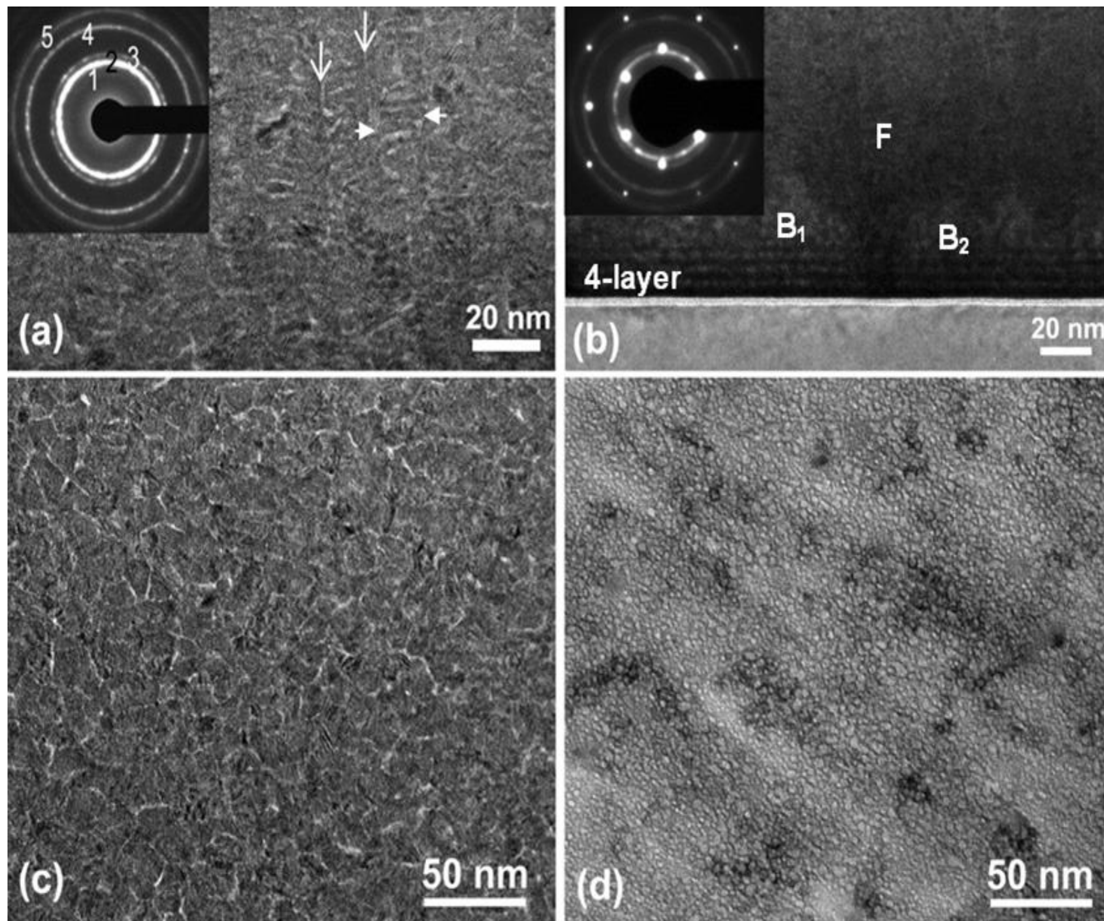

Figure 3.5 (a) and (b) Bright-field cross-section TEM image and SAED (inset) of the T25S7 film and the film/Si substrate interface, respectively. (c) and (d) plan-view TEM image taken from the T25S7 film and the film/Si interface, respectively.

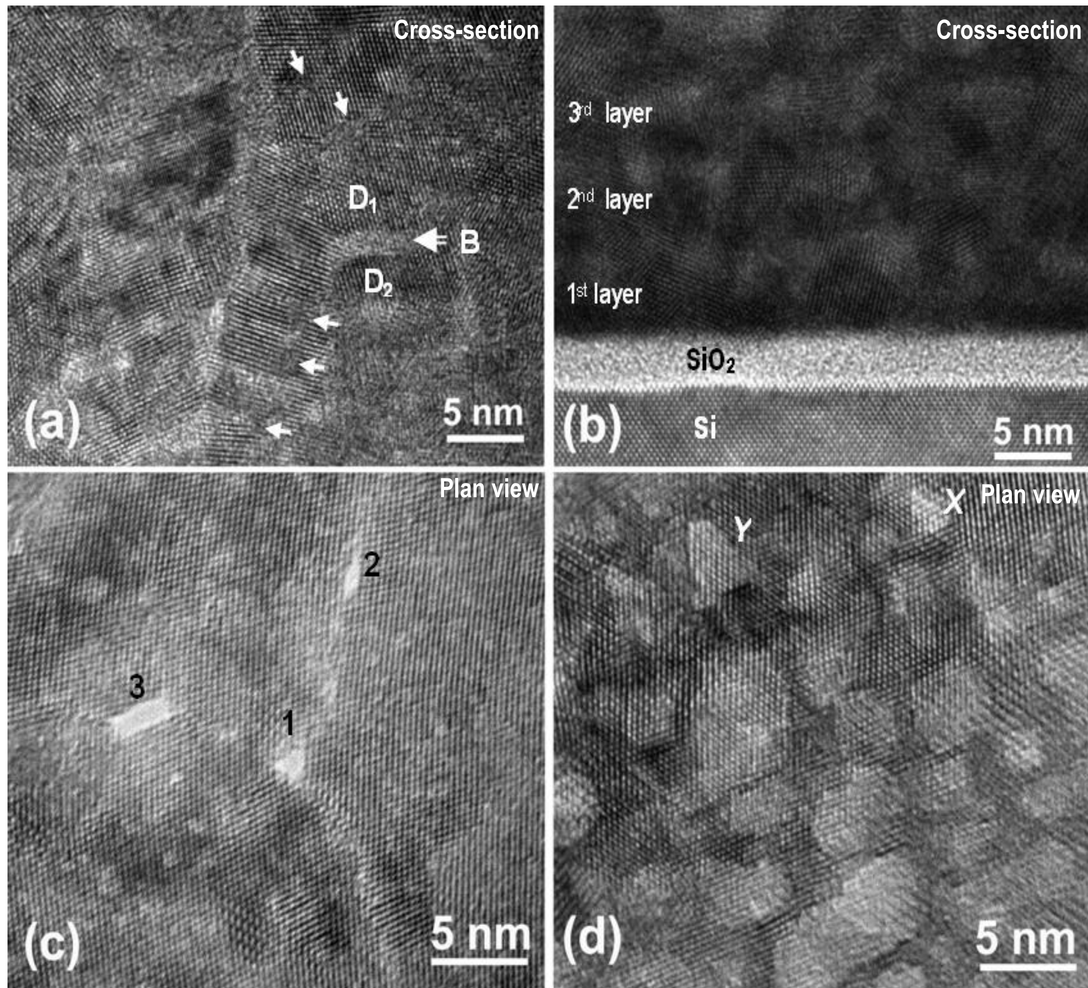

Figure 3.6 (a) and (b) cross-section HRTEM image of the T25S7 taken from the film and the film/Si interface, respectively. (c) and (d) Plan-view HRTEM image taken from an area in Fig. 3.5 (c) and (d), respectively.

Figure 3.6 (a) is a cross-section HRTEM image taken from column structure. The nano domains in the multilayered columnar structures (such as D_1 and D_2) are separated by a distorted crystal structure caused by defects, i.e., dislocations or disordered amorphous region (such as B). From cross-section TEM image Fig 3.6 (b), the multilayer structures are clearly seen just formed above interface. Those nanoparticles seem to possess a uniform grain size of ~ 5nm, much smaller than that in film area away from the interface. The boundaries (bright

contrast) between the layers are defect/boundary rich regions with low-density structures. Figs. 3.6 (c) and (d) are plan-view HRTEM images, which were taken from an area in Fig. 3.6(c) and (d), respectively. Nano-cavities can be clearly seen in these two images. Fig 3.6 (c) shows presence of nano-cavities (i.e., 1, 2 and 3) with a size of < 2nm at the grain boundaries as well as within the grains. Fig. 3.6 (d) is a HRTEM image taken from an area shown in Fig. 3.6 (b) presenting clear evidence of the presence of nanoscale regions with lower density (bright regions). HRTEM image of the bright regions (such as X and Y) clearly exhibit different characteristics from the surrounding structure. Such a difference is well known due to the difference of the sample thickness over the area, as can be confirmed by HRTEM image simulation. It can also be noticed that the grain structure in Fig. 3.6 (d) has a significantly larger size than that formed in the multilayered regions in Fig. 3.6 (b).

3.4.2 T200S54 and T200S18 sample

Films T200S54 and T200S18 exhibited a grain structure separated by thin boundaries as shown by the plan-view TEM images in Figs. 3.7 (a) and (b). The grain boundaries possess a uniform thickness. The HfO_2 grains in T200S54 film have an average size of ~46 nm, larger than those in T200S18 (~38 nm). Figs. 3.7 (c) and (d) are SAED patterns taken from film T200S54 and T200S18, respectively. The diffraction rings 1, 2, 3, 4, 5, 6, 7 and 8 in Fig. 3.7 (c) have a lattice spacing of 5.02 Å, 3.71 Å, 3.15 Å, 2.83 Å, 2.59 Å, 2.33 Å, 2.18 Å and 2.03 Å which can be determined to be the (100), (011), ($\bar{1}11$), (111), (200), (012), ($\bar{1}21$) and (121) or

(112) of the m-HfO_2 (PDF #: 01-075-6426) [35], respectively. The diffraction rings 1, 2, 3, 4, 5 and 6 in Fig. 3.7 (d) have the same lattice spacing as those in Fig. 3.7 (c) indicating that the T200S18 film has also a m-HfO_2 structure. The intensity of the diffractions in Fig. 3.7 (c) doesn't exhibit clear inhomogeneity over the rings indicating that there is no texture in film T200S54. However, the diffraction rings 3 and 5 in Fig. 3.7 (d) exhibit clear and strong inhomogeneity in intensity. Roughly, half of the symmetric quarter of the rings 3 and 5 in Fig. 3.7 (d) show diffractions attesting to the presence of texture in the T200S18 film.

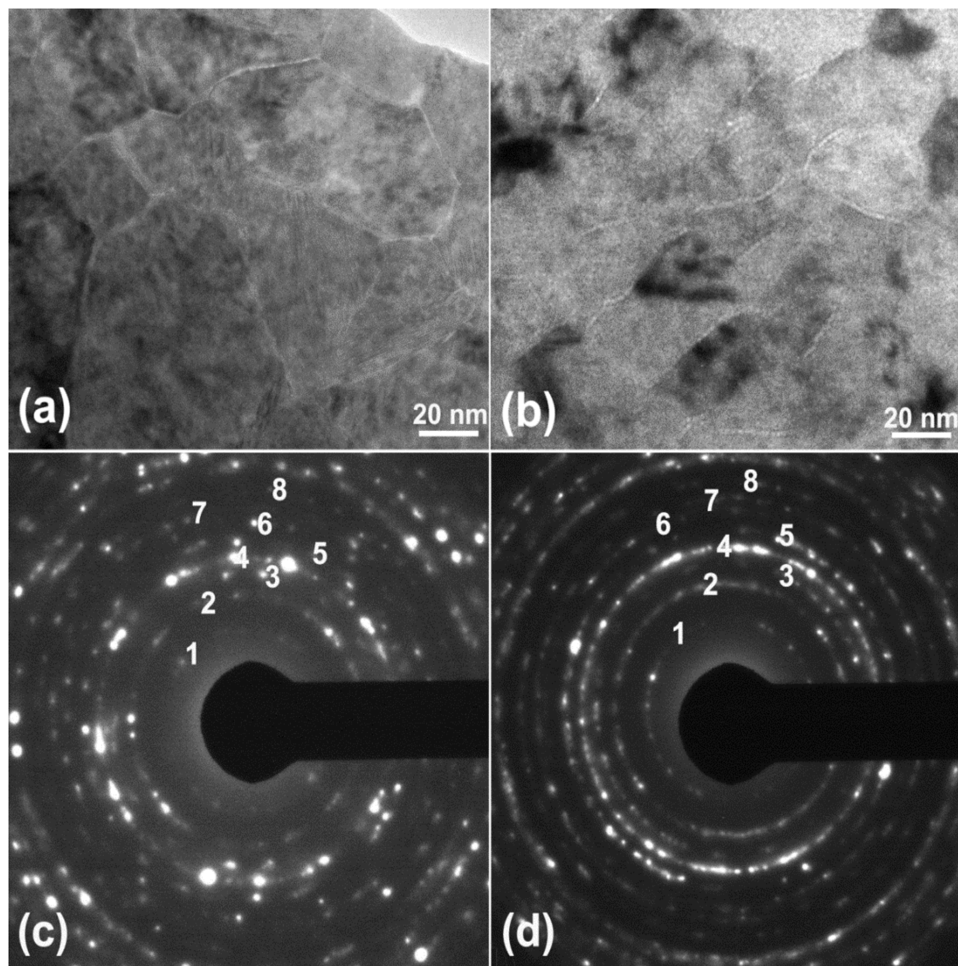

Figure 3.7(a) and (b) Plan-view TEM image, (c) and (d) SAED pattern of the T200S54 and T200S18 film, respectively.

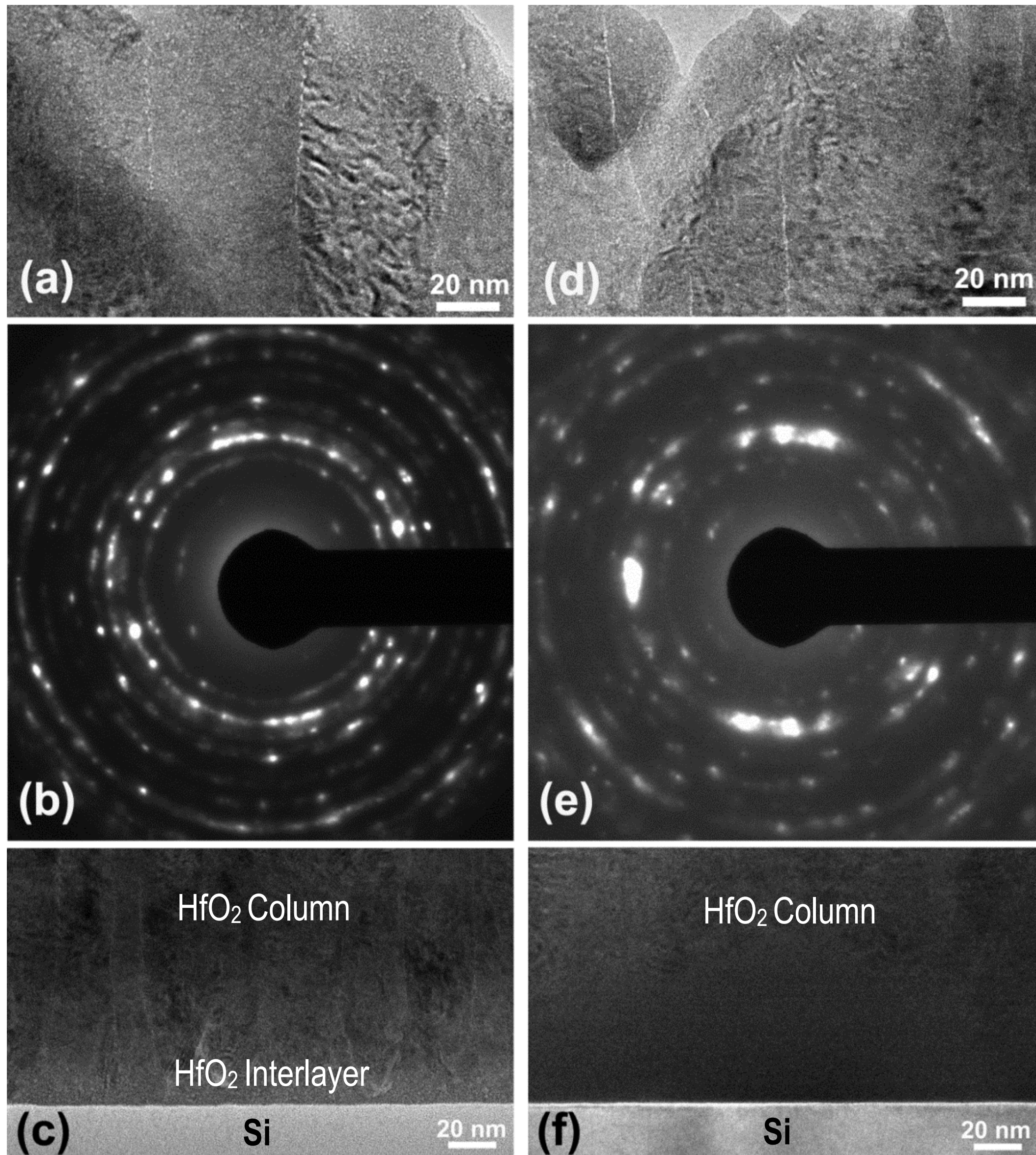

Figure 3.8 (a) and (d) Cross-section TEM image of the HfO_2 film taken from T200S54 and T200S18, respectively. (b) and (d) SAED pattern taken from the HfO_2 film in T200S54 and T200S18, respectively. (c) and (f) Cross-section TEM image of the film/Si interface in T200S54 and T200S18, respectively.

Fig. 3.8 (a) is a typical cross-section TEM image of the T200S54 film taken from an area away from the Si substrate presenting columnar structures with a column width of ~46 nm. Fig. 3.8 (b) is a SAED pattern taken from the HfO_2 columnar structures. Similar to Fig. 3.7 (c),

no strong inhomogeneous distribution of diffraction intensity along the rings was observed further confirming the absence of texture in this film. Observations revealed the presence of a HfO_2 interlayer just above the interface with the Si substrate before the formation of the columnar structure, Fig. 3.8 (c). The interlayer has a continuous homogenous structure and a hilly interface with respect to the columnar structure with a thickness of ~10 nm.

Figs. 3.8 (d) and (f) are typical cross-section TEM images of film T200S18 taken from an area away and close to the Si substrate, respectively. The T200S18 film possesses also a columnar structure, similar to T200S54. The interlayer in the T200S18 film is, however, much thicker than that in T200S54 with a thickness of ~55 nm. Fig. 3.8 (e) is a SAED pattern taken from the HfO_2 columnar structures in the T200S18 film showing strong inhomogeneous distribution of diffraction intensity along the rings further indicating formation of texture in the HfO_2 columnar structures.

Fig. 3.9 (a) is a cross-section HRTEM image of the T200S54 HfO_2 film showing two columnar structures (C_1 and C_2) and a boundary in between. It was observed that each column has a single crystal structure regardless of the formation of lower density nanoscale regions within each grain. The interface between the HfO_2 interlayer and Si substrate in T200S54 is shown by the HRTEM image in Fig. 3.9 (b). The HfO_2 interlayer is composed of a nanocrystalline structure with a size of several nm and is well attached to the Si substrate. Fig. 3.9 (c) is a magnified cross-section TEM image of T200S18 film showing the HfO_2 interlayer,

columnar structure layer and their interface. Contrary to the columnar structure area (C_0), a high population of lower density nanoscale regions were observed in the interlayer region (I). However, the interlayer region (I) is a highly crystalline structure despite the high population of the lower density regions, Fig. 3.9 (d). The crystal size in region (I) in T200S18 is in the tens of nm, much larger than that in T200S54, Fig. 3.9 (b). It is interesting to note that an abrupt drop in the frequency of these nanoscale regions occurs across the boundary from region I to C_0, Fig. 3.9 (d).

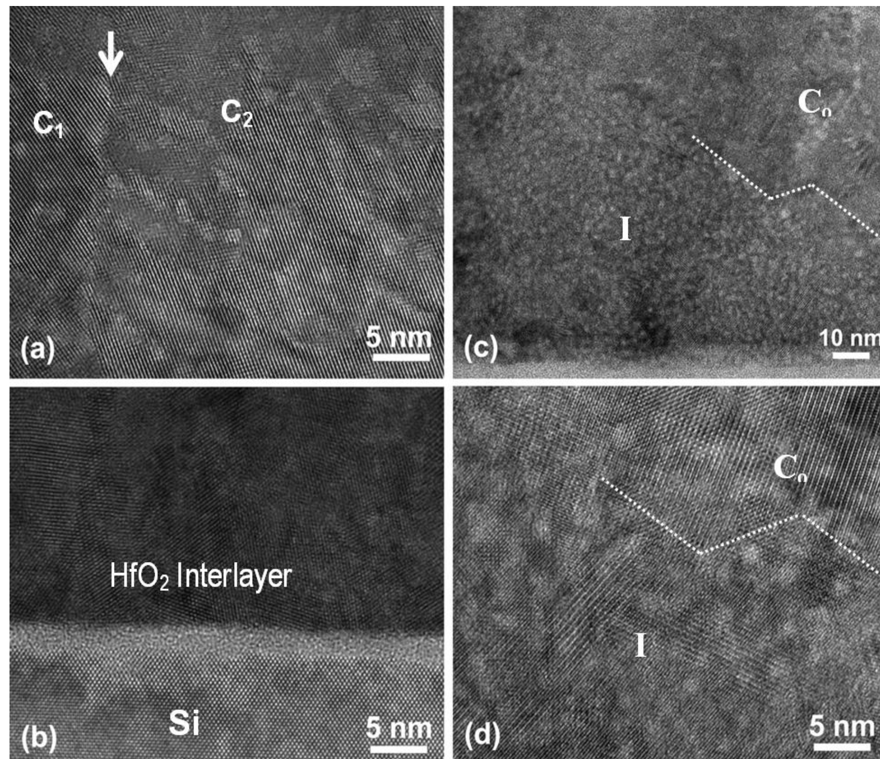

Figure 3.9 (a) and (b) Cross-section HRTEM image of the HfO_2 film and film/Si interface in T200S54, respectively. (c) Magnified cross-section TEM and (d) HRTEM image of the interface between the HfO_2 columnar structure and the interlayer in T200S18.

3.4.3 T200S7 and T100S7 sample

The microstructure of T200S7 and T100S7 films is presented by the plan-view TEM images shown in Figs. 3.10 (a) and (b). The grains in these films are separated by distinct boundaries instead of atomically thin boundaries. After examining a large number of grains, the average size for film T200S7 and T100S7 was ~24 nm and ~21 nm, respectively. More details of the grain structure is shown by the HRTEM images in Fig. 3.11. Well-defined and low-density boundaries with a thickness of ~1 nm are evident in the grain structure. SAED pattern analysis from the T200S7 film, revealed the same m-HfO_2 structure as in the films T200S54 and T200S18. Fig. 3.10 (c) is a SAED pattern taken from a plan-view TEM foil of the T100S7 film. Some differences can be observed in this pattern compared to those shown in Figs. 3.7 (c) and (d). The lattice spacing of the diffraction rings 1, 2, 3, 5, 6, 7 and 8 measured from Fig. 3.10 (c) is 5.10 Å, 3.64 Å, 3.15 Å, 2.56 Å, 2.22 Å, 2.04 Å and 1.82 Å, respectively. The most intense diffraction ring 4 is actually composed of two sub-rings with a d-spacing of 2.96 Å (inner ring, 4a)) and 2.83 Å (outer ring, 4b). The diffractions rings in Fig. 3.10 (c) cannot be indexed by a single phase. Comprehensive studies of SAED patterns show that the T100S7 film possesses both monoclinic and orthorhombic HfO_2 phases. Fig. 3.10 (d) depicts a comparison of the SAED patterns taken from the T200S7 (left) and T100S7 (right) film. A list of the d-spacing measured from the SAED patterns of the four films and the relevant data of the m-HfO_2 (PDF #: 01-075-6426) and o-HfO_2 (PDF #: 01-070-2832) is given in Table 3.4. All diffraction rings for the

T200S7 film (left of Fig. 3.10 (d)) can be indexed by m-HfO_2. Diffraction rings 1, 2, 3, 4b, 5, 7, 8 for the T100S7 film (right of Fig. 3.10 (d)) can be indexed by m-HfO_2, while diffraction rings 1, 2, 4a, 5, 6, 7, 8 can be indexed by o-HfO_2. In other words, diffraction rings 1, 2, 5, 7, 8 are common for both m-HfO_2 and o-HfO_2, while rings 3 and 4b uniquely belong to m-HfO_2 phase, and rings 4a and 6 belong to o-HfO_2.

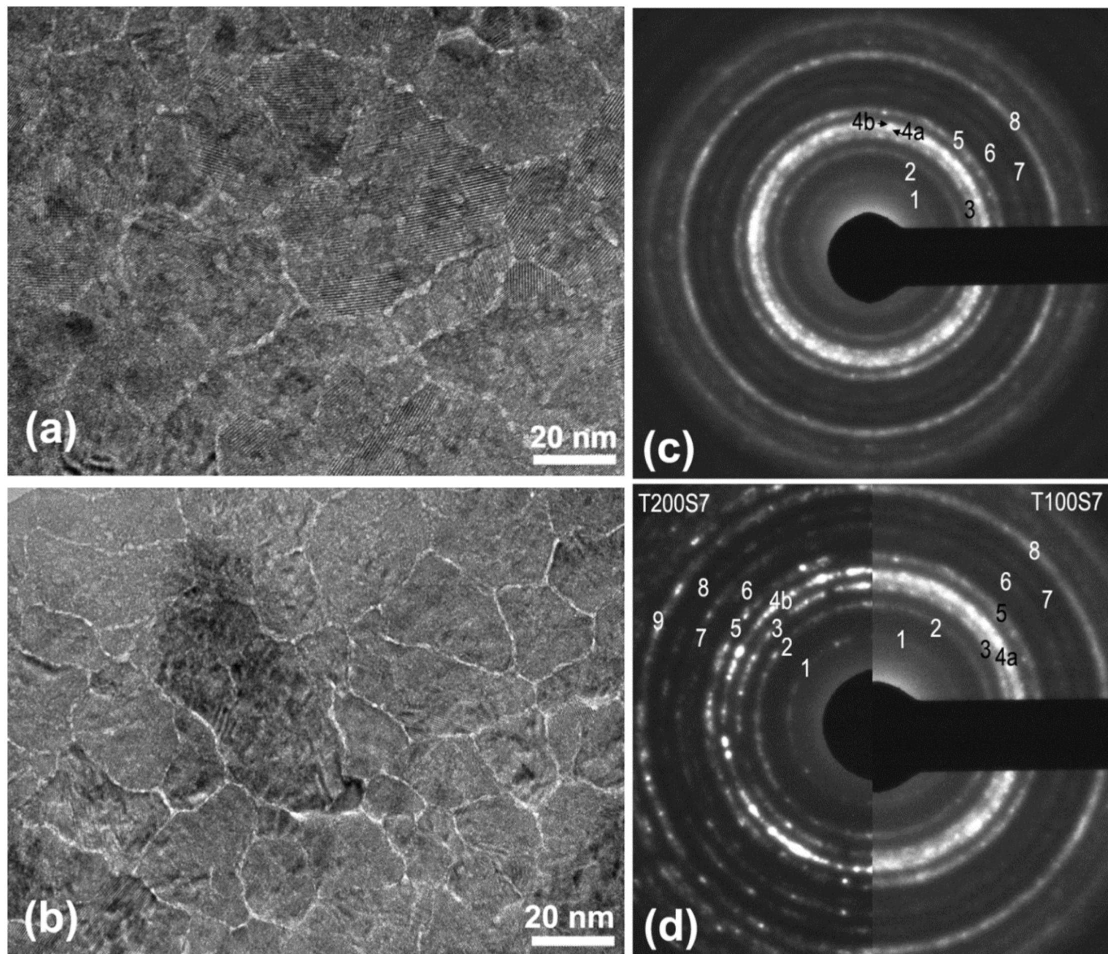

Figure 3.10 (a) and (b) Plan-view TEM image for T200S7 and (b) T100S7, respectively. (c) SAED pattern of the T100S7 film in a plan-view TEM foil. (d) Comparison of SAED pattern for the T200S7 and T100S7 film.

m-HfO_2		T200S54 / T200S18		T200S7		T100S7		o-HfO_2	
h k l	d (Å)	Diff. Ring	d (Å)	Diff. Ring	d (Å)	Diff. Ring	d (Å)	d (Å)	h k l
1 0 0	5.050	1	5.02	1	5.02	1	5.10	5.007	1 0 0
0 1 1	3.676	2	3.71						
1 1 0	3.612			2	3.62	2	3.64	3.616	1 1 0
-1 1 1	3.146	3	3.15	3	3.10	3	3.15		
						4a	2.96	2.942	1 1 1
1 1 1	2.825	4	2.83	4	2.79	4b	2.83		
0 2 0	2.584	5	2.59	5	2.55	5	2.56	2.529	0 0 2
0 1 2	2.332	6	2.33	6	2.31				
						6	2.22	2.258	2 1 0 / 1 0 2
-1 2 1	2.165	7	2.18	7	2.16				
1 2 1	2.052	8	2.03			7	2.04	2.062	2 1 1
1 1 2	2.012			8	2.01				
-1 2 2	1.793			9	1.79	8	1.82	1.818	0 2 2

Table 3.4 List of the d-spacing of the m-HfO_2, o-HfO_2, and the measured values from the SAED patterns of the T200S54, T200S18, T200S7 and T100S7.

Figs. 3.11 (a) and (b) are cross-section TEM images showing the presence of a columnar structure in these films away from the Si substrate similar to the previous two films. Figs. 3.11 (c) and (d) are SAED patterns taken from film T200S7 and T100S7, respectively, presenting strong inhomogeneous intensity distribution along the diffraction rings indicative of texture formation. The line profiles along the vertical direction passing through the center of the SAED (i.e. film growth direction) in Figs. 3.11(c) and (d) show diffractions similar to the XRD patterns of the T200S7 and T100S7 film, respectively. For example, the diffraction rings *a*, *b*, *c* and *d* in Fig. 3.11 (c) correspond to (110), ($\bar{1}11$), (111) and (002) of m-HfO_2. Diffraction rings *b*

and *d* show much stronger intensity than *a* and *c* at the intersection with the vertical dash line, in a good agreement with the XRD of the T200S7 film. Similarly, the intersection of ring *c* with the vertical line in Fig. 3.11 (d) depicts higher intensity than that of *a* and *d*, but lower than that of *b,* in a good agreement with the XRD of the T100S7 film.

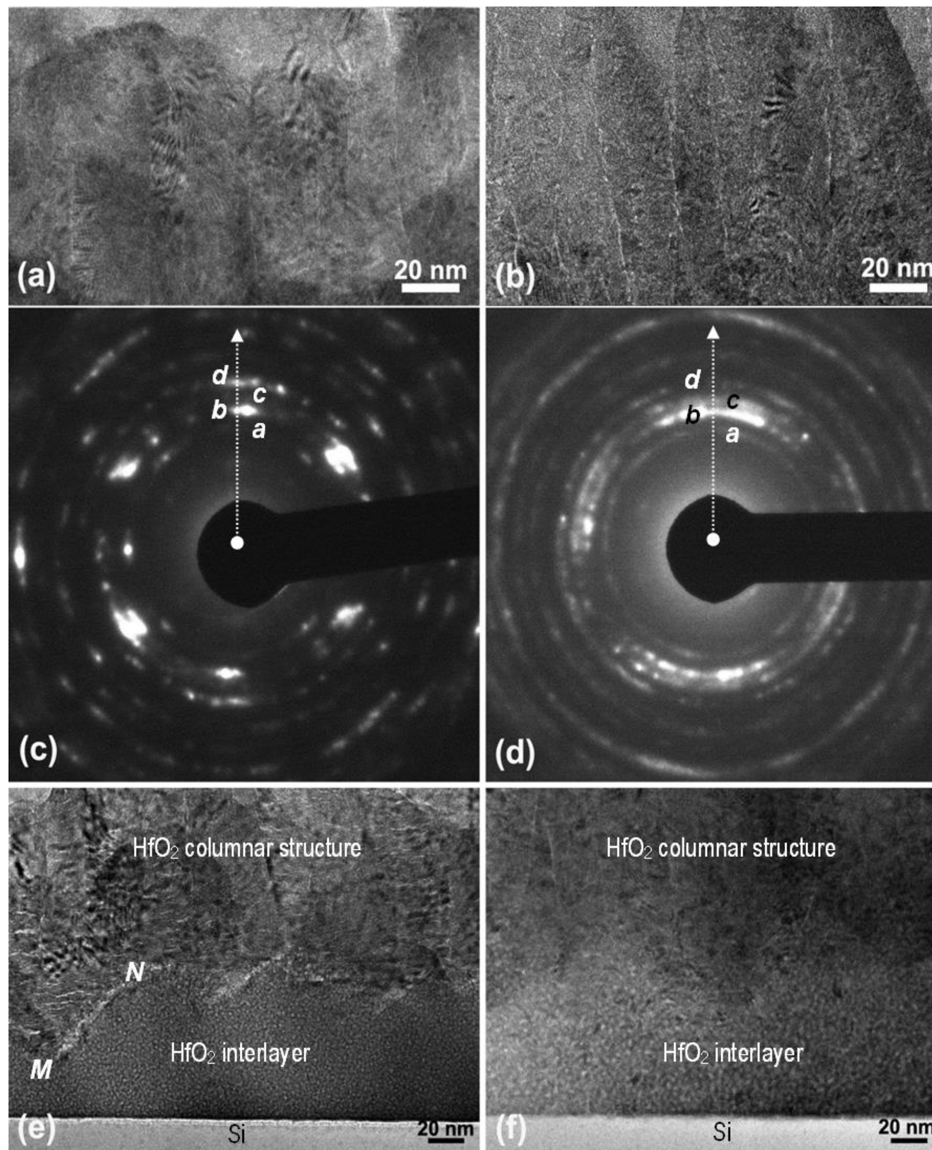

Figure 3.11 (a, c) and (b, d) Cross-section TEM image and SAED pattern of the HfO_2 film from T200S7 and T100S7, respectively. (e) and (f) TEM image of the film/Si interface for T200S7 and T100S7, respectively.

Figs. 3.11 (e) and (f) show the interlayer structure between the Si substrate and the columnar structure in film T200S7 and T100S7, respectively. Both interlayers show a continuous homogenous structure and a hilly interface with respect to the columnar structure. Both interlayers possess a similar thickness with an average value of ~60 nm.

Fig. 3.12 (a) is a cross-section HRTEM image of the T200S7 film presenting columnar structures and well defined boundaries. The lattices within or around the two regions marked by "*" are either highly distorted or disordered. The spots marked by "x" correspond to point defects that were likely produced by dislocations. Fig. 3.12 (b) is a cross-section HRTEM image of the T200S7 film showing atomic structure near the interface (white dot line) between the HfO_2 interlayer and columnar structure layer. Similar to the previous films, a high population of lower density nanoscale regions were observed in the interlayer, while their number was drastically reduced in the columnar region. Fig. 3.12 (c) is a HRTEM image of the interlayer/columnar structure boundary marked as M-N in Fig. 3.11 (e). The interface appears brighter while the lattice fringes in the columnar structure extended to the interlayer region without interruption after crossing the interface. Such contrast difference between the interface and surrounding structures is due to the mass variation of the sample indicating the lower density present at the interface. Fig. 3.12 (d) is a HRTEM image of the interface between the HfO_2 interlayer and Si substrate in T100S7 film. Similar to the previous films, the HfO_2 interlayer

is composed of a distribution of lower density nanoscale regions with a size of several nm up to 10 nm.

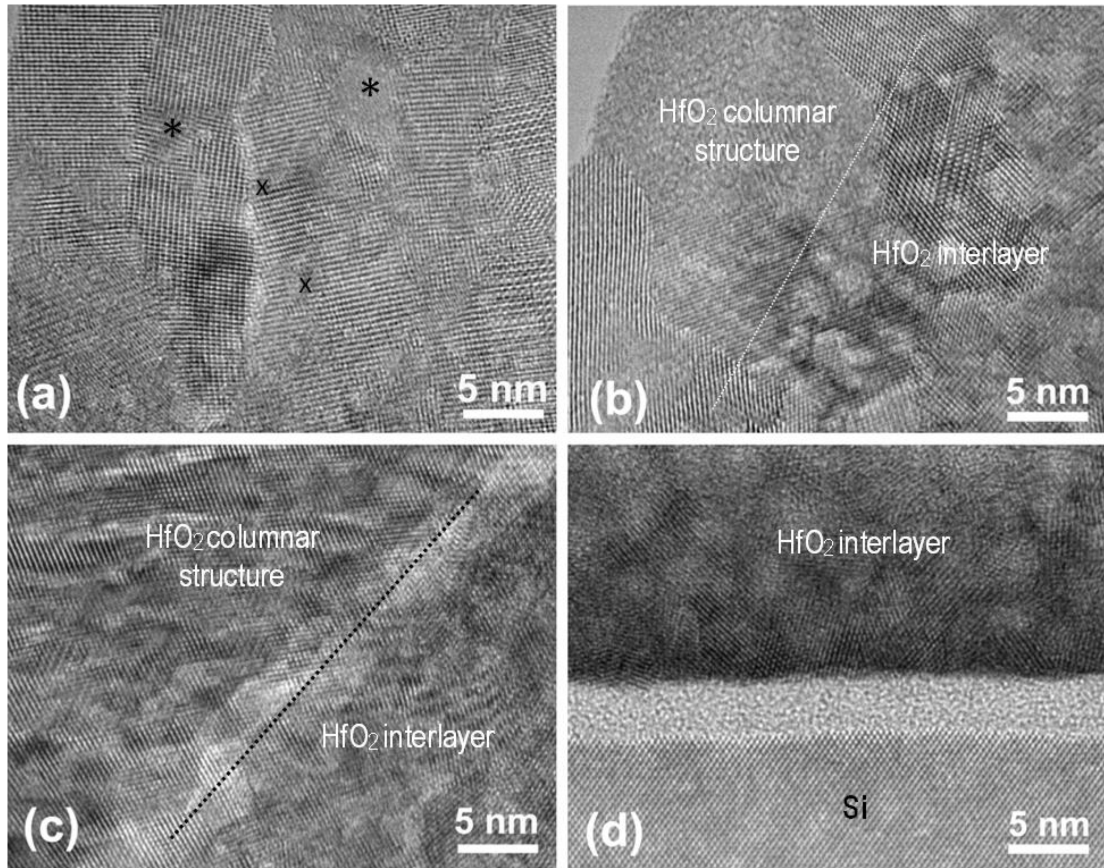

Figure 3.12 (a) Cross-section HRTEM image of the HfO_2 film in T200S7. (b) and (c) HRTEM image of the interface between HfO_2 columnar structure and HfO_2 interlayer in T200S7. (d) HRTEM image of the interface between the HfO_2 interlayer and Si in T100S7.

3.5 Influence of deposition parameters on microstructure and properties

The five HfO_2 films were deposited in vary voltage pulse durations (t_1) from 25 μs to 200 μs and averaged target power density (<S_d>) from 7.2 Wcm^{-2} to 54 Wcm^{-2}. This will enable us to discover the relationship between the deposition parameters, microstructure and the film properties, as discussed in the following. Figure 3.13 (a) shows comparison for column width

versus voltage pulse duration (t_1) and target power density ($<S_d>$). In following discussion, our five samples were divided in to two group. The first group consists of T200S54, T200S18 and T200S7 film, which were deposited using the same voltage pulse duration (t_1) but different target power density ($<S_d>$). The column width decreases while target power density ($<S_d>$) decreases.

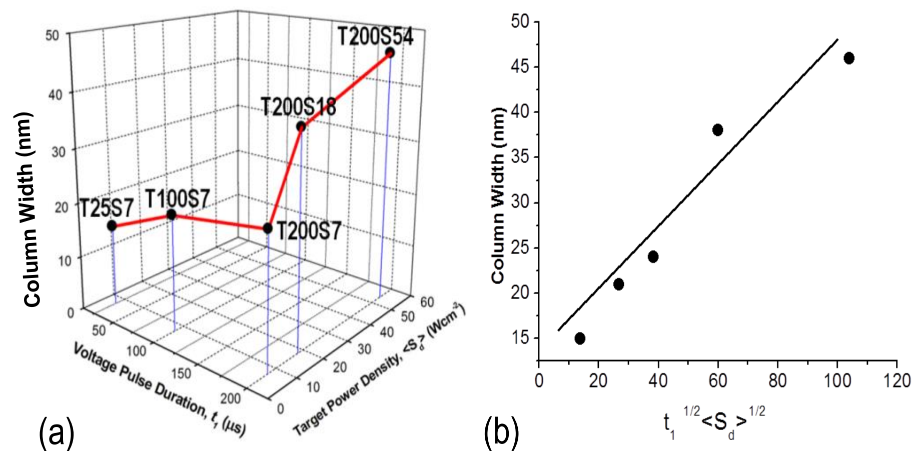

Figure 3.13 (a) Variation of column width in the HfO_2 thin films as a function of voltage pulse duration (t_1) and target power density ($<S_d>$). (b) Variation of column width with

The second group consists of T25S7, T100S7 and T200S7 film, which the films were deposited using the same target power density ($<S_d>$) but different voltage pulse duration (t_1). The column width decreases with decreasing voltage pulse duration (t_1). However, the impact of changing voltage pulse duration (t_1) to the column width is not as significant as the target power density ($<S_d>$). For example, changing t_1 from 200 μs to 100μs, only a small change was seen for the column width between T100S7 sample and T200S7 sample. After a comprehensive study, we found a linear relationship between the column width and $t_1^{1/2}<S_d>^{1/2}$ and the result was presented in figure 3.13 (b).

Another comparison diagram for interlayer thickness versus voltage pulse duration (t_1) and target power density (<S_d>) was presented in figure 3.14. From figure 3.14 (a), a clear effect by <S_d> is shown by the present findings. The films deposited using the same t_1, such asT200S54, T200S18andT200S7, shows that reducing <S_d> results in increase of the thickness of the interlayer. Furthermore, an effect by varying $t_1$with smaller <S_d> values (T25S7 and T100S7) on the promote formation of a thinner interlayer in figure 3.14 (a) is also seen. The T25S7, T100S7 and T200S7 films have same<S_d> but different t_1. For the samples with low t_1 (T25S7 and T100S7), increase t_1 will increase interlayer thickness.

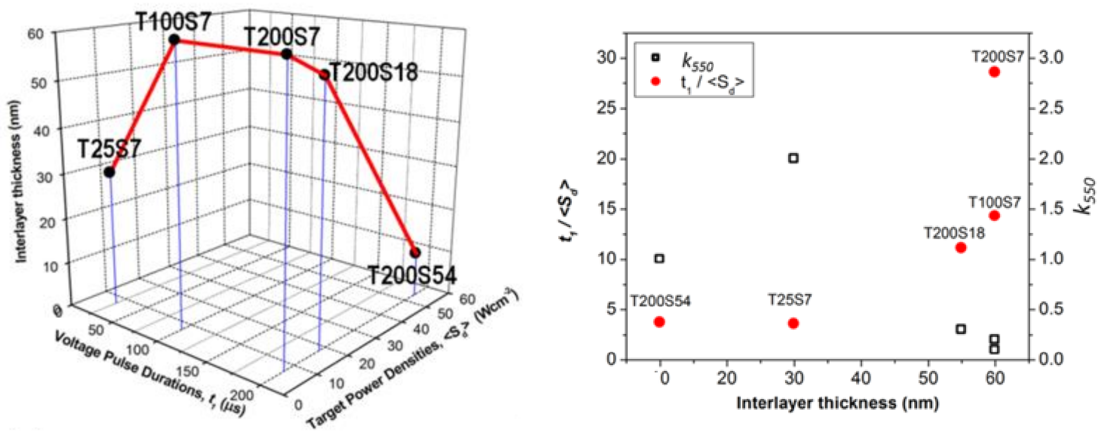

Figure 3.14 (a) Variation of interlayer thickness in the HfO_2 thin films with voltage pulse duration (t_1) and target power density (<S_d>). (b) Variation of k_{550} with t_1/<S_d> and interlayer thickness.

Fig. 3.14 (b) presents the variation of the interlayer thickness as a function of t_1/<S_d>. The graph suggests that an exponential type relationship may exist between t_1/<S_d> and interlayer thickness. This relationship is not understood at present. Furthermore, it is not clear

why a different interlayer thickness is needed under the various processing conditions for the initiation of columnar growth process.

Another interesting observation is that the HfO_2 crystalline in the films prepared with small $t_1/\langle S_d \rangle$ value (T200S54, T25S7) are distributed with their crystallographic direction randomly oriented and no texture was formed in the films. While the films prepared with large $t_1/\langle S_d \rangle$ value (T200S18, T200S7, T100S7) exhibit texture. This can be attributed to long depositions under low energies that both favor a columnar growth.

Chapter 4

CONCLUSION

HfO_2 films were deposited on Si substrates using High-power impulse magnetron sputtering process. The effect of the voltage pulse duration, t_1, and averaged power density, $\langle S_d \rangle$, on their microstructure was studied by HRTEM. Five HfO_2 films were prepared with (1) T25S7: t_1 = 25 μs, $\langle S_d \rangle$ =7.6 Wcm^{-2}; (2) T100S7: t_1 = 100 μs, $\langle S_d \rangle$=7.2 Wcm^{-2}; (3) T200S7: t_1 = 200 μs, $\langle S_d \rangle$ =7.3 Wcm^{-2}; (4) T200S18: t_1 = 200 μs, $\langle S_d \rangle$ =18 Wcm^{-2} and (5) T200S54: t_1 = 200 μs, $\langle S_d \rangle$ =54 Wcm^{-2}. All films were composed of an interlayer with the Si substrate followed by a nano-columnar structure layer. The nano-cavities fully occupied in interlayer and the hilly boundary was formed between columnar structure layer and interlayer.

T200S54 and T200S18 films consist of nano-columnar structures (~46 nm and ~38 nm wide) separated by abrupt sharp boundaries, T200S7 and T100S7 films have nano columnar structures (~24 nm & ~21 nm wide) separated by rough boundaries (average ~ 1 nm thick) of high-density nano cavities and T25S7 film has multilayered (~3 nm thick) nano columnar structures (~15 nm wide) on the top of the interlayer.

Different condition of voltage pulse duration, t_1, influences a lot on crystal structure. m-HfO_2 structure prepared with a large t_1 (T200S54, T200S18 and T200S7) and o-HfO_2 structure will form when sample prepared with a small t_1 (T25S7). A mixture of m- and o-HfO_2 phases prepared with T100S7. Decreasing $\langle S_d \rangle$ and t_1, was found to reduce the width of the columns,

increase the thickness of the grain boundaries and thickness of the interlayer. For mechanical property, the films with m-HfO_2 structure have the highest hardness (17.6-17.0 GPa).

References

[1] K. Kukli, M. Ritala, T. Sajavaara, J. Keinonen, M. Leskelä. Chemical Vapor Deposition 8:5 (2002) 199-204

[2] J. Aarika, A. Aidlaa, H. Mändara, V. Sammelselgb, T. Uustarea. Journal of Crystal Growth 220 (2000) 105-113

[3] X. Zhao, D. Vanderbilt Physical Review B, Volume 65, 233106

[4] Z. He, W. Wu, H. Xu, J. Zhang, Y. Tang. Vaccum 81 (2006) 211-214

[5] S.C. Chen, T.C. Chang, H.H. Su, P.C. Yang, J Lu, H.C. Huang, D.S. Gan, N.J. Ho, Y. Shi. Materials Letters 63 (2009) 1914-1916

[6] M. Alvisia, S. Scaglioneb, S. Martellic, A. Rizzod, L. Vasanellia. Thin Solid Films 354 (1999) 19-23

[7] M.F. Al-Kuhaili. Optical Materials 27 (2004) 383–387

[8] V. Pervak, F. Krausz, A. Apolonski, Hafnium oxide thin films deposited by reactive middle-frequency dual-magnetron sputtering, Thin Solid Films 515 (2007) 7984–7989.

[9] R.K. Jain, Y.K. Gautam, V. Dave, A.K. Chawla, R. Chandra, A study on structural, optical and hydrophobic properties of oblique angle sputter deposited HfO_2 films, Appl. Surf. Sci. 283 (2013) 332–338.

[10] K. Sarakinos, D. Music, S. Mráz, M. To Baben, K. Jiang, F. Nahif, et al., On the phase formation of sputtered hafnium oxide and oxynitride films, J. Appl. Phys. 108 (2010) 014904.

[11] G. Aygun, A. Cantas, Y. Simsek, R. Turan, Effects of physical growth conditions on the structural and optical properties of sputtered grown thin HfO_2 films, Thin Solid Films 519 (2011) 5820–5825.

[12] T.J. Bright, J.I. Watjen, Z.M. Zhang, C. Muratore, A.A. Voevodin, Optical properties of HfO_2 thin films deposited by magnetron sputtering: From the visible to the far-infrared, Thin Solid Films 520 (2012) 6793–6802.

[13] M. Szymanska, S. Gieraltowska, L. Wachnicki, M. Grobelny, K. Makowska, R. Mroczynski, Effect of reactive magnetron sputtering parameters on structural and electrical properties of hafnium oxide thin films, Appl. Surf. Sci. 301 (2014) 28–33.

[14] M. Audronis, A. Matthews, K. Juškevičius, R. Drazdys, Unlocking the potential of voltage control for high rate zirconium and hafnium oxide deposition by reactive magnetron sputtering, Vacuum 107 (2014) 159–163.

[15] I. Safi, Recent aspects concerning DC reactive magnetron sputtering of thin films: a review, Surf. Coat. Technol. 127 (2000) 203–218.

[16] J. Musil, P. Baroch, J. Vlček, K.H. Nam, J.G. Han, Reactive magnetron sputtering of thin films: Present status and trends, Thin Solid Films 475 (2005) 208–218

[17] W.D. Sproul, D.J. Christie, D.C. Carter, Control of reactive sputtering processes, Thin Solid Films 491 (2005) 1–17.

[18] J. Vlček, A. Belosludtsev, J. Rezek, J. Houška, J. Čapek, R. Čerstvý, S. Haviar, High-rate reactive high-power impulse magnetron sputtering of hard and optically transparent HfO_2 films, Surf. Coat. Technol. doi:10.1016/j.surfcoat.2015.08.024

[19] J. Wang, H.P. Li, R. Stevens, Hafnia and hafnia-toughened ceramics, J. Mater. Sci. 27 (1992) 5397–5430.

[20] K. Matsumoto, Y. Itoh, T. Kameda, EB-PVD process and thermal properties of hafnia-based thermal barrier coating, Sci. Technol. Adv. Mater. 4 (2003) 153–158.

[21] J. Singh, D.E. Wolfe, R.A. Miller, J.I. Eldridge, D.M. Zhu, Tailored microstructure of zirconia and hafnia-based thermal barrier coatings with low thermal conductivity and high hemispherical reflectance by EB-PVD, J. Mater. Sci. 39 (2004) 1975–1985.

[22] A.J. Waldorf, J.A. Dobrowolski, B.T. Sullivan, L.M. Plante, Optical coatings deposited by reactive ion plating, Appl. Opt. 32 (1993) 5583–5593.

[23] M. Fadel, O.A. Azim M., O.A. Omer, R.R. Basily, A study of some optical properties of hafnium dioxide (HfO_2) thin films and their applications, Appl. Phys. A Mater. Sci. Process. 66 (1998) 335–343.

[24] J. Ni, Y. Zhu, S. Wang, Z. Li, Z. Zhang, B. Wei, Nanostructuring HfO_2 thin films as antireflection coatings, J. Am. Ceram. Soc. 92 (2009) 3077–3080.

[25] P. Torchio, A. Gatto, M. Alvisi, G. Albrand, N. Kaiser, C. Amra, High-reflectivity HfO_2/SiO_2 ultraviolet mirrors, Appl. Opt. 41 (2002) 3256–3261.

[26] M.F. Al-Kuhaili, Optical properties of hafnium oxide thin films and their application in energy-efficient windows, Opt. Mater. 27 (2004) 383–387.

[27] J.H. Choi, Y. Mao, J.P. Chang, Development of hafnium based high-k materials - A review, Mater. Sci. Eng. R Reports. 72 (2011) 97–136.

[28] J. Bohlmark, M. Lattemann, J.T. Gudmundsson, A.P. Ehiasarian, Y. Aranda Gonzalvo, N. Brenning, U. Helmersson. The ion energy distributions and ion flux composition from a high power impulse magnetron sputtering discharge, thin solid films 515 (2006) 1522-1526.

[29] J. Alami, P.O.A. Persson, D. Music, J.T. Gudmundsson, J. Bohlmark, U. Helmersson, Ion-assisted physical vapor deposition for enhanced film properties on nonflat surfaces, J. Vac. Sci. Technol., A23 (2005), p. 278

[30] W.D. Sproul, D.J. Christie, D.C. Carter, The reactive sputter deposition of aluminum oxide coatings using high power pulsed magnetron sputtering (2004) 47th Annual Technical Conference Proceedings of the Society of Vacuum Coaters, , pp. 96-100.

[31] A.P. Ehisarian, W.-D. Munz, L. Hultman, U. Helmersson, I. Petrov, High power pulsed magnetron sputtered CrNx films, Surf. Coat. Technol., 163–164 (2003), p. 267

[32] A. Anders, J. Andersson, A. Ehiasarian, High power impulse magnetron sputtering: Current-voltage-time characteristics indicate the onset of sustained self-sputtering,Journal of Applied Physics 102, 113303 (2007)

[33] S. Bolz, New coating technology achieves optimal adhesion. In: CemeCon Facts. Nr. 35, S. 11–12.
[34] J. Alamia, P Eklundb, J. Emmerlichb, O. Wilhelmssonc, U. Janssonc, H. Högbergb, L. Hultmanb, U. Helmerssona, High-power impulse magnetron sputtering of Ti–Si–C thin films from a Ti_3SiC_2 compound target, Thin Solid Films 515 (2006) 1731–1736
[35] Powder Diffraction File™, PDF-2, Release 2009, ICDD, International Centre for Diffraction Data, Newton Square, PA, USA.